MICROFLUIDICS FOR SINGLE MOLECULE DETECTION AND MATERIAL PROCESSING

A Dissertation

by

SUNG MIN HONG

Submitted to the Office of Graduate Studies of
Texas A&M University
in partial fulfillment of the requirements for the degree of

DOCTOR OF PHILOSOPHY

August 2012

Major Subject: Electrical Engineering

MICROFLUIDICS FOR SINGLE MOLECULE DETECTION AND MATERIAL PROCESSING

A Dissertation

by

SUNG MIN HONG

Submitted to the Office of Graduate Studies of
Texas A&M University
in partial fulfillment of the requirements for the degree of

DOCTOR OF PHILOSOPHY

Approved by:

Chair of Committee,	Jun Kameoka
Committee Members,	Chin B. Su
	Kuang-An Chang
	Raffaella Righetti
Head of Department,	Costas N. Georghiades

August 2012

Major Subject: Electrical Engineering

ABSTRACT

Microfluidics for Single Molecule Detection and Material Processing. (August 2012)

Sung Min Hong, B.A., Kyung Hee University;

M.S., Kyung Hee University

Chair of Advisory Committee: Dr. Jun Kameoka

In the cancer research, it is important to understand protein dynamics which are involved in cell signaling. Therefore, particular protein detection and analysis of target protein behavior are indispensable for current basic cancer research. However, it usually performed by conventional biochemical approaches, which require long process time and a large amount of samples. We have been developed the new applications based on microfluidics and Raster image Correlation spectroscopy (RICS) techniques.

A simple microfluidic 3D hydrodynamic flow focusing device has been developed for quantitative determinations of target protein concentrations. The analyte stream was pinched not only horizontally, but also vertically by two sheath streams by introducing step depth cross junction structure. As a result, a triangular cross-sectional flow profile was formed and the laser was focused on the top of the triangular shaped analyte stream. Through this approach, the target protein concentration was successfully determined in cell lysate samples.

The RICS technique has been applied to characterize the dynamics of protein 53 (p53) in living cells before and after the treatment with DNA damaging agents. P53

tagged with Green Fluores-cent Protein (GFP) were incubated with and without DNA damaging agents, cisplatin or eptoposide. Then, the diffusion coefficient of GFP-p53 was determined by RICS and it was significantly reduced after the drug treatment while that of the one without drug treatment was not. It is suggested that the drugs induced the interaction of p53 with either other proteins or DNA. This result demonstrates that RICS is able to detect protein-protein or protein-DNA interactions in living cells and it may be useful for the drug screening.

As another application of microfluidics, an integrated microfluidic platform was developed for generating collagen microspheres with encapsulation of viable cells. The platform integrated four automated functions on a microfluidic chip, (1) collagen solution cooling system, (2) cell-in-collagen microdroplet generation, (3) collagen microdroplet polymerization, and (4) incubation and extraction of the microspheres. This platform provided a high throughput and easy way to generate uniform dimensions of collagen microspheres encapsulating viable cells that were able to proliferate for more than 1 week.

DEDICATION

To my parents and my family

ACKNOWLEDGEMENTS

I would like to thank and express my sincerest gratitude towards my advisor, Dr. Jun Kameoka, for his unrelenting guidance and support throughout the course of my research. I would also like to thank my committee members, Dr. Su, Dr. Chang and Dr. Righetti, for their valuable insights and suggestions on my research.

Next, I am deeply grateful to Dr. Hung, Dr. Yamaguch, and Dr. Chou at the Department of Molecular and Cellular Oncology, MD Anderson Cancer Center for their clinical and biological support.

Thanks also go to my friends, colleagues and the department staff at Texas A&M University. I also want to extend my gratitude to the staff at Cornell Nanoscale Facility for their help on device fabrication, and to the staff at Microscopy Imaging Center and Materials Characterization Facility at Texas A&M University.

Lastly and most importantly, I would like to express my love and deepest gratitude to my family for their endless love, encouragements, endurance, patience, and support. Without them, this could not be possible. Many thanks to my parents, Kwang-Woong Hong and Geum-Ja Kim who have always been very proud of all of my accomplishments, my wife and sons (Minjung Kim, Jihan Hong, and Seohan Hong), who have always been beside me all years long. Thank you for always being there for me.

NOMENCLATURE

SMD	Single Molecule Detection
NA	Numerical Aperture
APD	Avalanche Photo Diode
EOF	Electroosmotic Flow
RICS	Raster Image Correlation Spectroscope
DEP	Dielectrophoretic
PDMS	Poly (dimethylsiloxane)
SEM	Scanning Electron Microscope
FFT	Fast Fourier Transform
QD	Quantum Dot
FCS	Fluorescence Correlation Spectroscopy
GFP	Green Fluorescent Protein

TABLE OF CONTENTS

LIST OF FIGURES

LIST OF TABLES

1. INTRODUCTION

Breast cancer is a major disease in women in the United States. Annually, around 205,000 women are suffering from breast cancer.[1] Various techniques have been developed to reveal tumor-related proteins along the signal pathways, but many details still remain unclear due to limitations of current techniques.[2, 3]

In recent years, microfluidics has been extensively studied to handle small volume of samples. In order to control micro volume of fluid, micrototal analysis system (μ-TAS) or lab-on-a-chip (LOC) concepts have been developed and integrated in the various fields of biological and chemical assays.[4, 5] Hydrodynamic focusing is the one of efficient way of producing uniform sample stream in microfluidic channels by confining sample flow laterally via shear force of sheath flows. This techniques are widely used in the application of micro-flow cytometry or drug delivery system, such as single molecule reaction,[6] microfluidic cell sorter,[7] cell patterning,[8] and generation of monodisperse particles or polygonal water droplets.[9, 10] Conventionally, sample stream was formed a thin rectangular cross-sectional profile by neighboring sheath flows due to the horizontal shear force. While the horizontal flow confinement can be relatively easy to be achieved, vertical hydrodynamic focusing requires additional compartments or multiple protocols. For instance, some of 2D hydrodynamic focusing devices have been introduced so far to improve the vertical resolution.[10-13]

This dissertatation follows the style of *Applied Physics Letters*.

Although these devices allow horizontal and vertical focusing of sample stream, complex fabrication protocol and multiple PDMS layers assembly are necessary to fabricate devices.

In this dissertation, new approaches of multidisciplinary efforts were presented: the development of novel 3D hydrodynamic focusing for accurate quantitative protein detection, Raster Image Correlation Spectroscope (RICS) as a tool of drug screening, and a development of microfluidics platform for collagen microspheres generation (Figure 1).

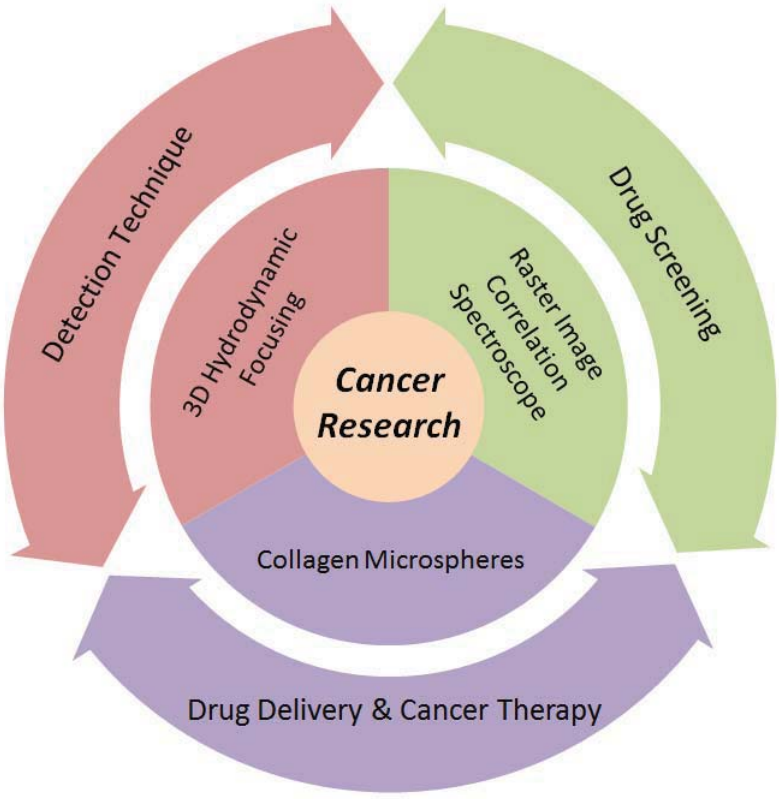

Figure 1. An overview of research

Specifically, Section 2 describes the simple structure of 3D hydrodynamic focusing device with step depth junction, which is able to demonstrate vertical and horizontal flow confinement effects. This confinement effect was experimentally confirmed by using a confocal microscope. Compared to other techniques, our device has several advantages, including straightforward structure (one sheath and sample inlet) and fast fabrication method via standard photolithography. In addition, microfluidic device is able to control the cross-sectional profile of sample stream by changing sheath and sample flow rates.

The work from Section 3 extends the RICS as a tool of drug screening. RICS can analyze the spatial fluctuation in the fluorescence signal, which is generated by the movement of fluorescence labeled molecules, to obtain molecular diffusion information. We have investigated the effects of DNA damaging agents, cisplatin and etoposide, on p53 dynamics in living HeLa cells by using RICS. After the drug treatment, the significant reductions of p53 mobility were observed compared to the one without drug treatment. Both cisplatin and etoposide induced DNA damage that stabilized and activated p53, resulting in the formation of the DNA-p53-transcription co-factors complex. Therefore, the results obtained by RICS explain the p53 dynamics in living cells.

In the Section 4, an integrated high-throughput microfluidic platform is introduced to generate collagen microspheres of uniform size and shape with high cell viability. Since this platform integrated the collagen microdroplet generation and the gelation functions on a chip, the time lag between these steps was sufficiently short so as

to avoid coalescence of microdroplets, resulting in highly uniform microspheres. Further, a novel microfluidic extraction approach was employed that considerably improved cell viability over that obtained with centrifugal extraction.

2. MICROFLUIDIC 3D HYDRODYNAMIC FOCUSING FOR RAPID PROTEIN CONCENTRATION ANALYSIS

2.1 Introduction

Over the past decade, single molecule detection (SMD) techniques have been incorporated with microfluidics systems[14-16] and studied for single molecule detections for DNA and fluorescent dyes.[17-19] For instance, DNA fragment sizing was demonstrated by using fluorescent signal detection in fused silica microfluidic channels and a high numerical aperture (NA) microscope objective lens.[20-22] DNAs were stained with the dimeric fluorescent intercalating dyes and electrokinetically flowed into the detection channel. Whenever DNA molecules passed through the detection spot, fluorescent photon was detected by the avalanche photo diode (APD). Since long DNA fragments were able to carry more fluorescent tags, length of DNAs could be identified by their fluorescent intensities from Gaussian photon histogram. Recently, these microfluidic SMD techniques have been expanded to the protein detection in cell lysate solutions.[23, 24] Although there were some successful single protein detections, fused silica based microfluidic device had difficulty to characterize protein concentration because of the fluctuation of electroosmotic flow (EOF) velocity. Proteins tend to adsorb on the surface of fused silica that caused surface charge instability.

The conventional 2D capillary flow focusing system with 50-200 μm width of pinched analyte flow have been developed for single molecular detection of fluorescent dye molecules.[25-27] In these approaches, low numerical aperture (NA) objective lens and high power laser were used to form a large laser spot to cover the width of capillary. On the other hand, larger laser spot would be a cause of the target molecules bleaching because of the longer residual time in the laser spot. In case of cell lysate sample solution, the target molecule signals would be inhibited by the auto-fluorescent from other molecules contained in a large detection volume.

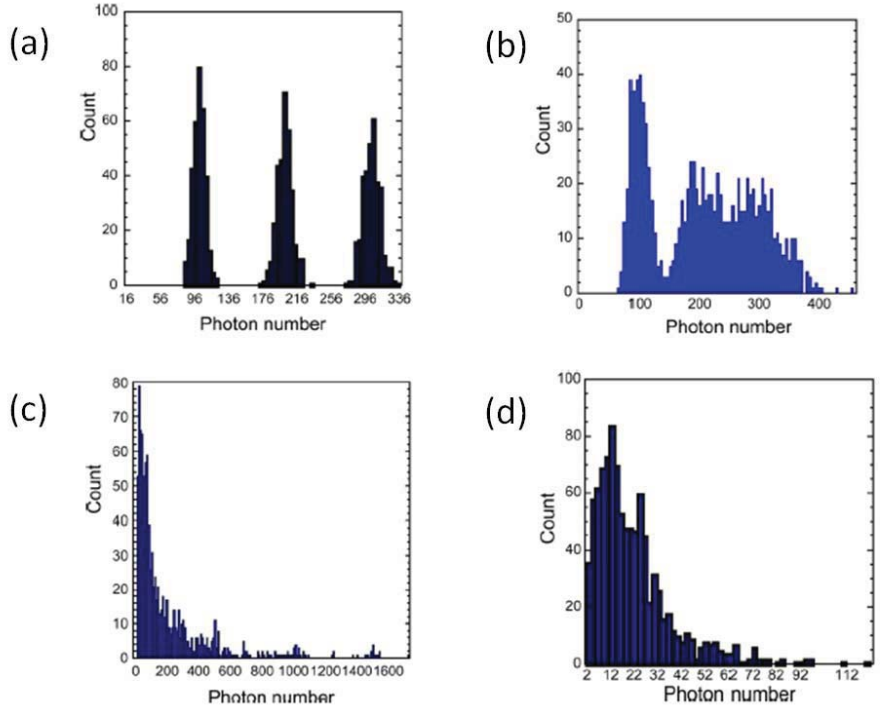

Figure 2. The distorted histograms from a wide fluidic channel. (a) no diffusion, (b) weak diffusion, (c) strong diffusion, (d) photonic noise in case of strong diffusion.[28]

As a result, the photon burst histogram was disturbed from normal Gaussian profile and provided inaccurate concentration measurements (Figure 2). Recently, the capillary flow focusing technique was implemented to microfluidics and has detected single molecules and fluorescent dyes.[29-33] The dimensions of analyte flow in microfluidic device were reduced to 20-50μm, but detection volumes were not significantly reduced. Therefore, the auto-fluorescent was influenced to photon burst histograms. The comparison of conventional technique (Western Blot) and our technique is shown in Table 1.

Table 1. Comparison of SMD techniques.

	Western Blot	Micro-channel SMD techniques	3D Hydrodynamic Focusing
Signal source	Ensemble of molecules	Single molecule	Single molecule
Sensitivity	Nano-gram	Picomolar	Picomolar
Processing time	3 days	2-3 min	2-3 min
Cost	High	High (channel fabrication cost)	Low
Quantitative information	No	Yes	Yes
Analysis method	Existence (band width & brightness)	Photon counts (distorted histogram)	Photon counts (Gaussian histogram)

So far, there have been no reports of protein concentration determination by using single molecule detection system. Accurate determination of protein concentration is important in cancer research to understand complex process of development and progression. Also, the Myc/MAX protein complex is a transcription regulator that controls various physiological functions such as cell proliferation, differentiation, metabolism and apoptosis.[34] More importantly, Myc/MAX complex are frequently upregulated in human cancer and plays a critical role in cancer development and progression.[34] Myc and MAX form a heterodimer and directly binds to specific DNA sequences to activate or repress gene transcription.[35] The expression levels of Myc and MAX in cells are critical determinants for multiple cellular functions. Therefore, in the present study, we chose the MAX protein as a model to further develop a novel protein detection system. This is the first time to determine the protein concentration by counting each protein. In order to detect accurate protein concentration, normal Gaussian distribution of photon burst distribution is necessary.[28] We have developed simple 3D hydrodynamic focusing devices to overcome current problems and improve the SMD accuracy for the protein concentration analysis. Our design can provide Gaussian photon burst distributions to determine the protein concentration by reducing significantly the detection volume.

2.2 Hydrodynamic Focusing Techniques

Several techniques of two dimensional (2D) Hydrodynamic Focusing have been introduced since 1998.[36-39] 2D hydrodynamic focusing technique allowed the sample to position on the center of channel. As a result, sample dispersion was minimized. However, it is difficult to detect a single molecule using conventional 2D hydrodynamic focusing because the conventional 2D hydrodynamic focusing in microfluidic channel formed a thin rectangular cross-sectional profile as shown in Figure 3. The height of fluidic flow is same as the vertical height of channel dimension. Therefore, two or more target molecules were detected at the detection volume due to the lack of vertical resolution.

In order to overcome the weakness of 2D hydrodynamic focusing, several 3D hydrodynamic focusing devices have been introduced to improve the vertical resolution.[10, 11, 40-43] Although these devices allow horizontal and vertical focusing of sample stream, some of limitations still exist such as vertical position control problem[44] and multiple PDMS layers assembly (Figure 4).[45, 46] Although, Mao et al. proposed a single layer 3D hydrodynamic focusing technique.[47] It requires high flow velocity to make Dean flow, which makes a difficulty of vertical position controlling.

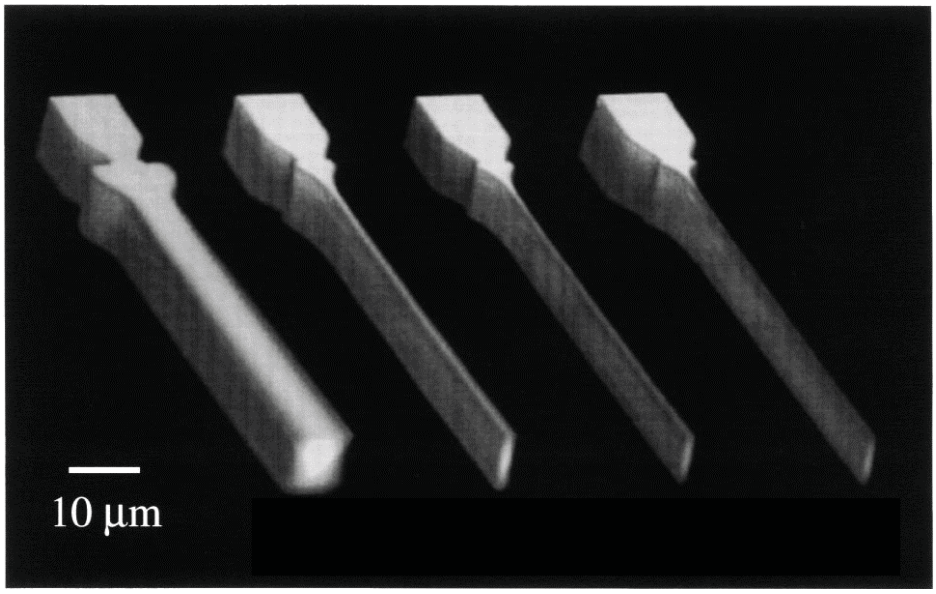

Figure 3. Confocal scanning microscopy images of typical 2D hydrodynamic focusing at the different flow conditions.[36]

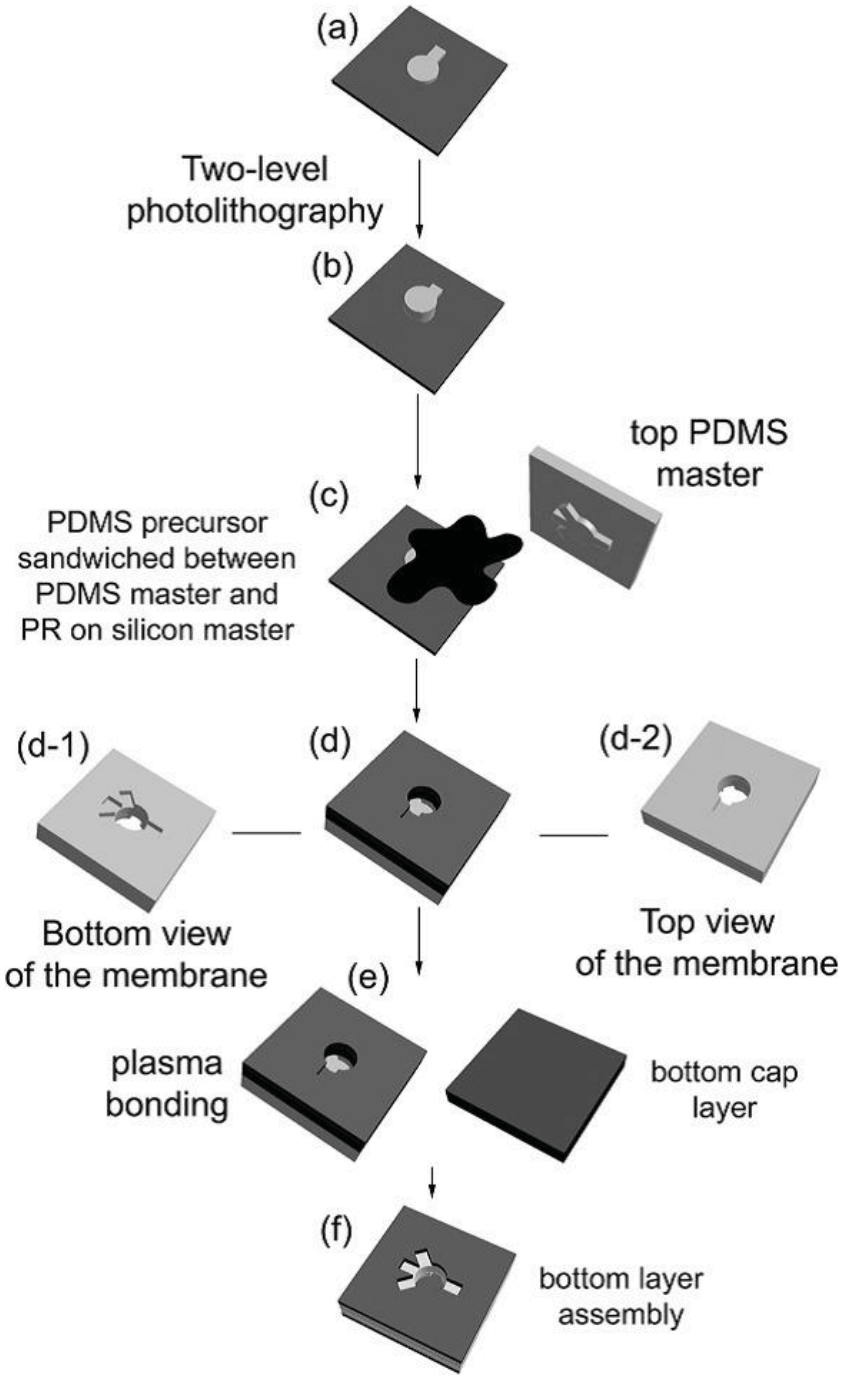

Figure 4. An example of procedure of the layer assembly for the 3D hydrodynamic focusing chip. [46]

2.3 Microfluidic Channel Fabrication

Microfluidic devices were fabricated on poly (dimethylsiloxane) substrate (PDMS; Dow Corning, Midland, MI) by standard micro-molding procedures.[48] Two lithographic processes were used to fabricate a mold of the shallow and deep channels on a silicon wafer separately. SU-8 2010 photoresist (Microchem Corp., Newton, MA) was spin-coated with the thickness of 10 μm on a silicon wafer and exposed by EV620 contact aligner. After the development process, the shallow channel was formed. Then, 50 μm thickness of SU-8 2050 (Microchem Corp., Newton, MA) was spin-coated on the smaller channel patterned silicon surface.

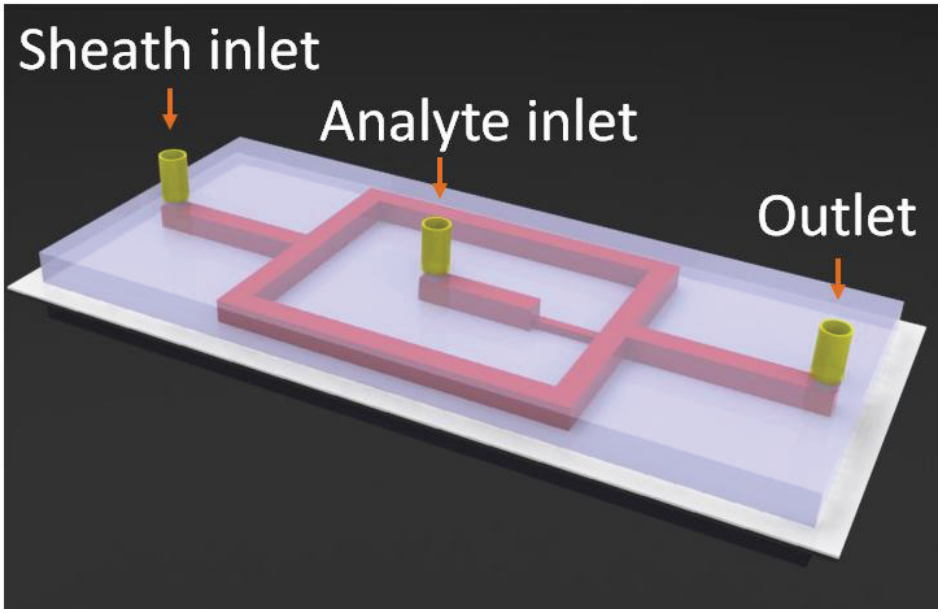

Figure 5. The schematic diagram of microfluidic channel. Chip-level view of the 3D hydrodynamic focusing device.

The second mask was aligned with the alignment markers made by the first lithography process. At this process, the shallow channel was connected to the deep channels to form the step junction structure. After the exposure and development processes, the micro-mold for microfluidic devices was made on the silicon wafer. Then, uncured PDMS mixture was dispensed over the lithographically patterned silicon mold and cured at 65 C° for 2 hours. Then, cured PDMS substrate was peeled off from the master silicon mold. The PDMS microchannel substrate was bonded to quartz cover slide glass (170 μm thickness) by oxygen plasma treatment for 30 seconds. Since most proteins are positively charged at pH 7, the PDMS channel was coated by polyethyleneimine (PEI), which is a positively charged polymer, to prevent protein absorption on channel wall. A schematic diagram of the 3D microfluidic flow focusing device was shown in Figure 5.

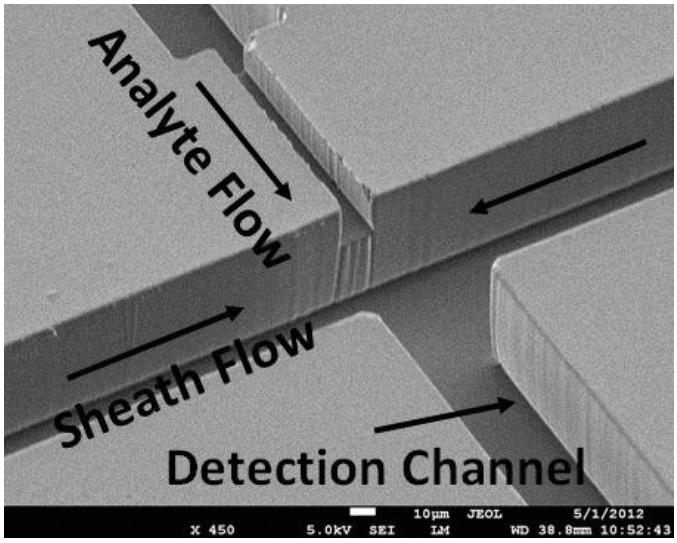

Figure 6. The SEM image of the cross junction area (scale bar: 10 μm).

This device mainly consisted of two different depths and widths of microchannels. The shallow channel (10 μm in depth and width) was connected with the deep sheath inlet channels (50 μm in depth and width) at the cross junction. Sheath and analyte streams were delivered into the main detection channel (50 μm in depth and width) by two separate syringe pumps (11 plus, Harvard Apparatus, Cambridge, MA) at various flow rates. A scanning electron microscope (SEM) image showed the sheath, the detection, and the analyte channels at the cross junction area (Figure 6).

2.4 Photon Burst Detection System

The microfluidic device was placed on the Nikon 2000 Inverted microscope stage as shown in Figure 7. Analyte and sheath streams were delivered through their inlets and 375 nm laser (16 mW) was focused through 60X water immersion objective lens at the top of the triangular shaped analyte stream, which was about 15 μm above the bottom of the main channel. The radius of laser spot was calibrated to 1.1 μm. whenever analyte molecules passed through the detection spot; they were excited and emitted fluorescent photon bursts.

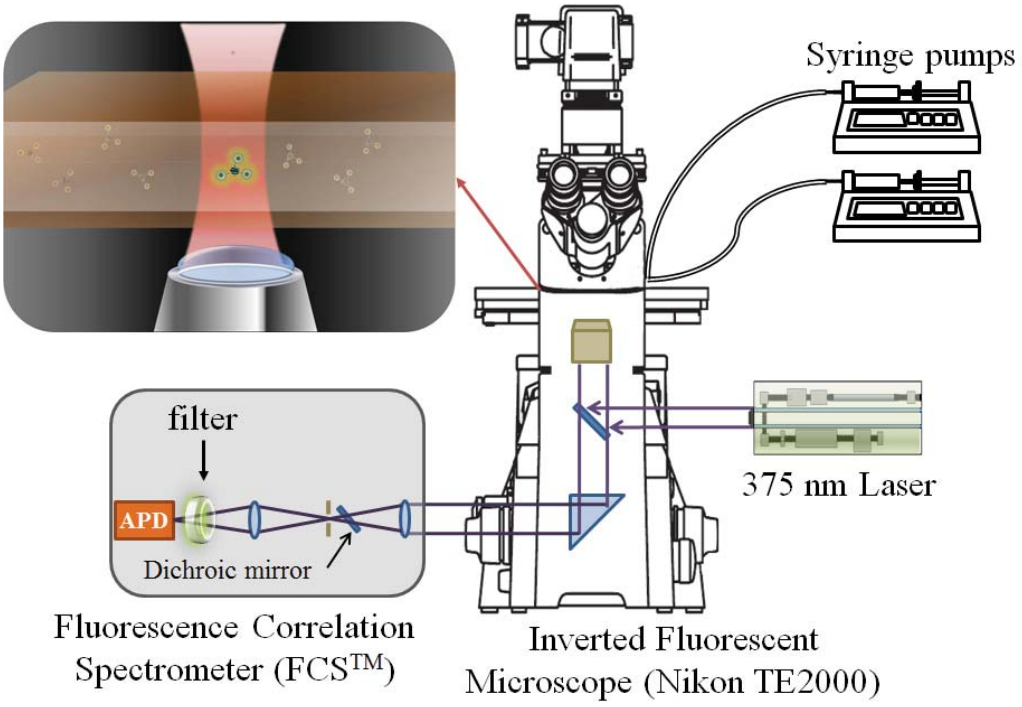

Figure 7. Experimental setup: syringe pumps delivered analyte and sheath flows to the microfluidic device. QDs were excited by 375 nm laser. Emitted fluorescent signals were detected by APD in photon burst detection system.

For all detections, five sets of raw photon burst data were recorded for 10 seconds each. The recorded raw photon burst data was smoothened by fast Fourier transform (FFT) filter[49] and the individual photon burst peaks higher than the noise level, which was determined by the blank solution, were defined as single molecule peaks. These peaks were plotted on the photon burst histogram which indicated the number of target molecules detected (Figure 8).

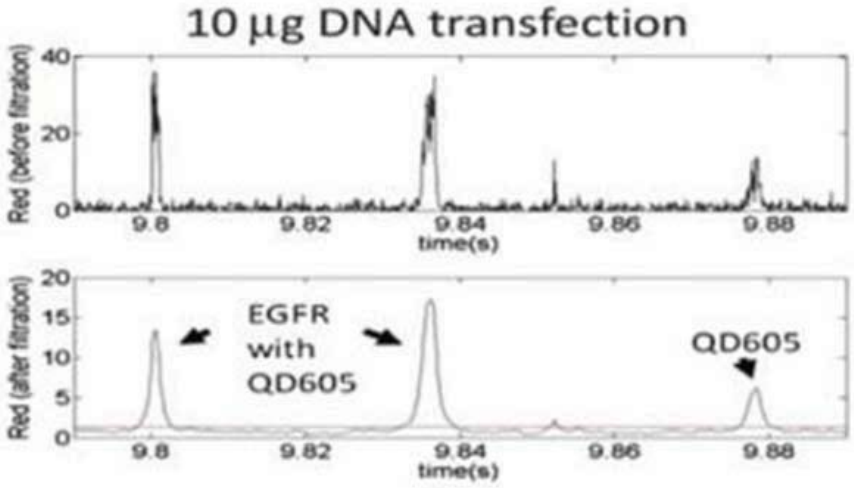

Figure 8. An example of FFT filtering of photon burst data. Upper: raw photon burst profile. Lower: photon burst signal profile after the FFT filtering process.[10]

2.5 Sample Protein Preparation

Quantum dot (QD)-conjugated anti-rabbit IgG secondary antibody was purchased from Invitrogen, Inc. In this solution, 1 µM concentration of QD525-antibody was suspended in 1 M betaine, 50 mM borate, pH 8.3 with 0.05% sodium azide solution. This solution was diluted with phosphate buffered saline (PBS) to a concentrations of 10 pM, 100 pM and 1 nM. HA-MAX expression plasmid or empty vector was transiently transfected in human embryonic kidney 293 (HEK-293) cells by using liposome. 24 hours after transfection, the cells with or without HA-MAX expression were harvested and lysed in RIPA buffer (50 mM Tris-HCl, 1% NP-40, 150 mM NaCl, 1 mM EDTA plus protease inhibitors). After measuring protein concentration, the cell lysates containing 100 µg total proteins were mixed in IP binding buffer (20 mM Hepes-KOH,

0.1 mM KCl, 2 mM $MgCl_2$, 15 mM NaCl, 0,2 mM EDTA, 1mM DTT, 10% glycerol). The HA-MAX protein was labeled with QD525-antibody through anti-HA rabbit polyclonal primary antibody and QD525-conjugated anti-rabbit IgG secondary antibody. The cell lysate from empty vector-transfected 293 cells that did not express HA-MAX was mixed with anti-HA polyclonal primary antibody plus QD525-conjugated anti-rabbit IgG secondary antibody and used as a control sample (Figure 9).

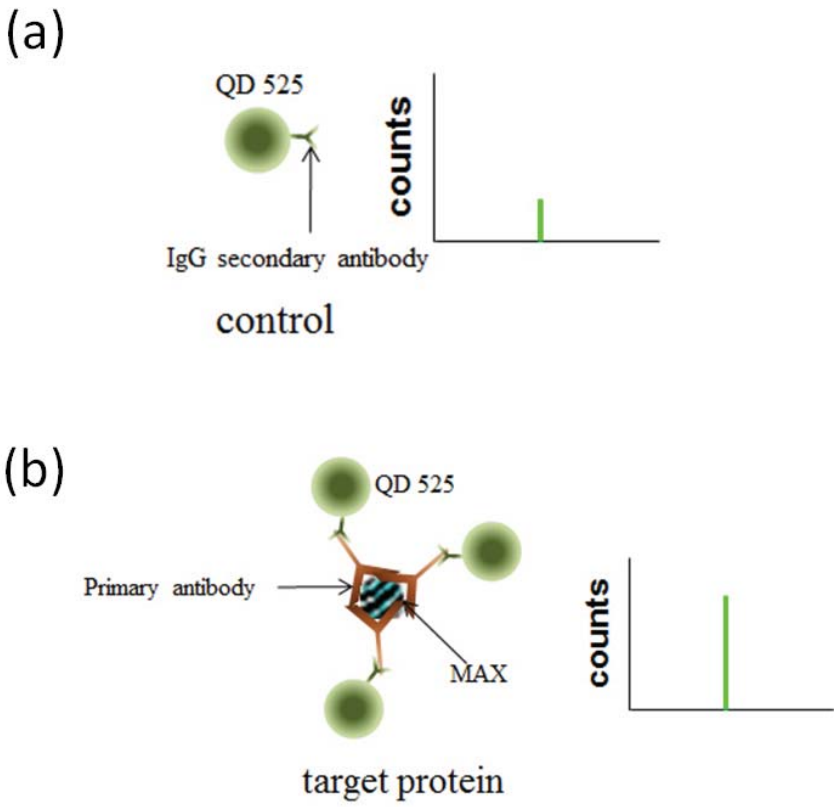

Figure 9. Sample protein preparation. (a) QD525 binds to MAX through primary antibody anti-HA. (b) MAX protein is associated with multiple QD525s due to anti-HA's polyclonal nature. Identification of target protein from free QD525 in cell lysate mixture based on photon counts.

2.6 Characterization of 3D Hydrodynamic Flow Focusing

The confocal fluorescent microscopy (Olympus FV1000) equipped with air-cooled 543nm HeNe laser was used to characterize the 3D hydrodynamic flow focusing. Rhodamine B resolved in phosphate buffered saline (PBS) solution was injected through the analyte inlet and DI water was pumped through the sheath inlet to form the 3D flow focusing. The cross-sectional images were obtained at the 100 μm apart from the cross junction with different analyte and sheath flow conditions. The confocal microscope had 60X water immersion objective (NA=1.2) and Z-stacked series of fluorescent images were taken at 0.53 μm intervals. In addition, a top view and a side view of the analyte stream in the detection channel were also characterized.

2.7 Results and Discussion

2.7.1 Characterization of Analyte Flow Profile

In order to characterize the 3D hydrodynamic flow focusing of the analyte stream, the cross-sectional images were obtained by using the confocal microscope. 1μM concentration of Rhodamine B dissolved in PBS solution was induced into the analyte inlet and DI water was pumped through the sheath stream inlet. The analyte flow rate ($V_{Analyte}$) and the sheath flow rate (V_{Sheath}) were independently controlled by two syringe pumps. The $V_{Analyte}$ was set to 1 μl/min and the V_{Sheath} was also controlled from 10 μl/min to 160 μl/min. Also, the cross sectional profiles were characterized at the different combinations of $V_{Analyte}$ and V_{Sheath} (data was not shown). Figure 10 (a) showed the cross sectional view, top view and side view of fluorescent images of the analyte

stream at the flow condition of $V_{analyte}$: 1 μl/min and to $V_{sheath:}$ 60 μl/min. Same as other flow conditions, the analyte stream was straight and uniform for 0.1 mm from the cross junction. Cross sectional images of the analyte stream with different flow conditions of analyte and sheath streams were shown at Figure 10 (b). From these images, it was obvious that the height of the analyte stream was reduced by increasing V_{sheath}, and the cross section of the analyte stream was generally deformed to a triangular shape. Because the depth of sheath channels was deeper than that of the analyte outlet channel, the analyte stream was pressured from three directions, *i.e.*, top to down, left to right and right to left as shown in Figure 10 (a). As shown in Figure 10 (b), the analyte stream showed the large cross sectional area at the lower sheath flow rate.

The sample flow cross-section diagram as a function of sheath and sample flow rates is shown in Figure 11. The sample flow rate was increased from 1 μl/min to 3 μl/min at 0.5 μl/min steps and sheath flow rate was also changed according to sample flow rate increments. As mentioned earlier, in all cases, the cross-sectional shapes of sample flow showed sharp triangle at the lower sheath flow rate and flat triangle at the higher sheath flow rate. Also, the areas of sample stream were exponentially decreased.

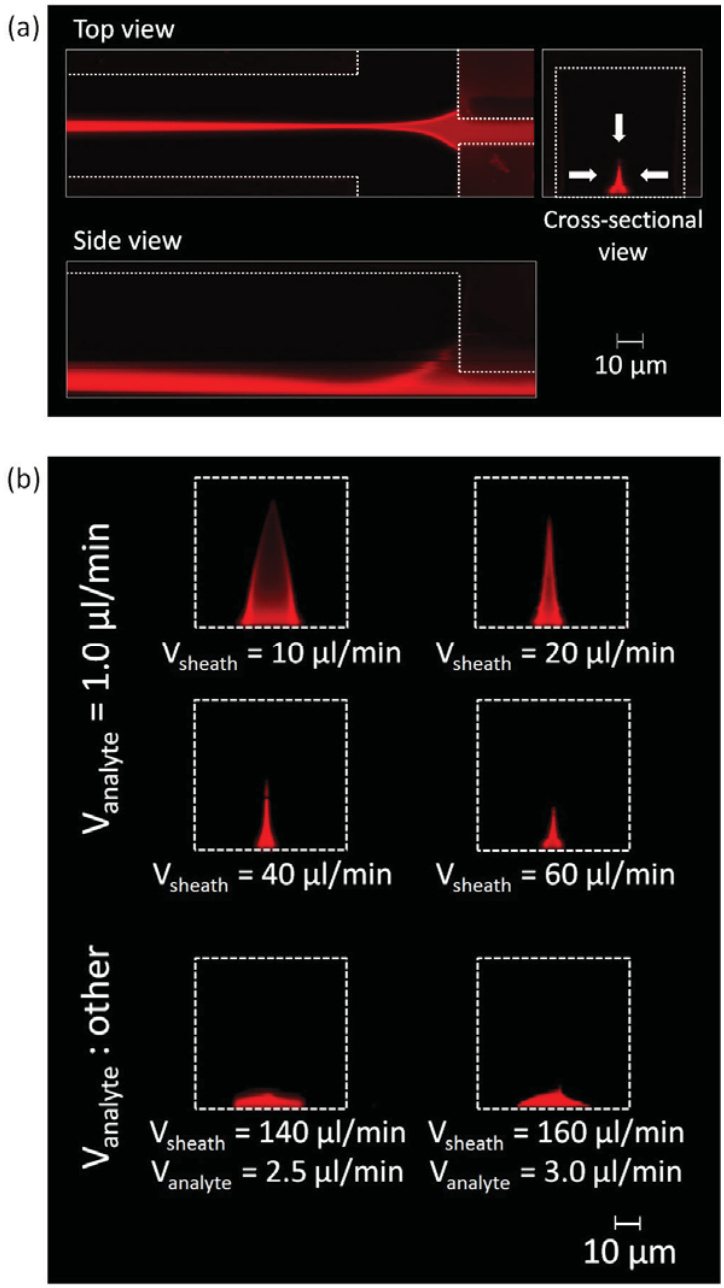

Figure 10. Analyzing flow profile. (a) The concept of 3D focusing mechanism. (b) The cross-sectional profiles of rodamine B flow with different analyte and sheath flow rate (white dotted line: the wall of the channel).

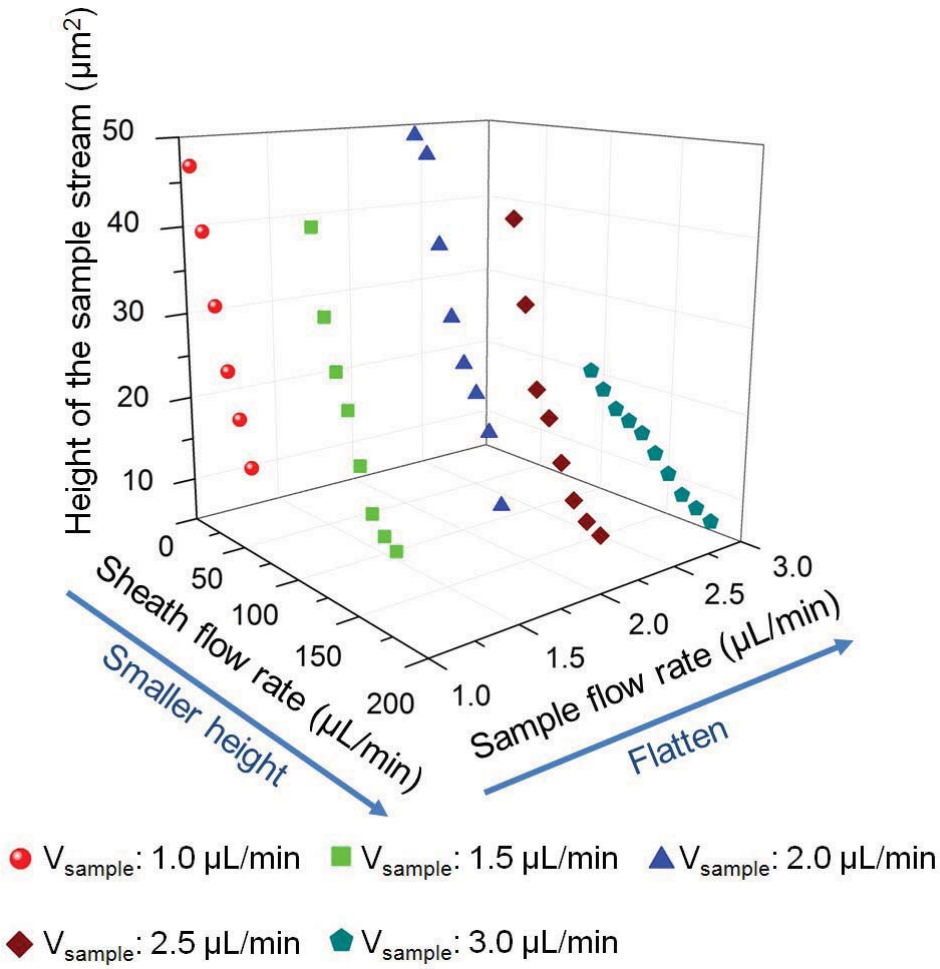

Figure 11. The cross-sectional profile diagram as a function of sheath and sample flow rates. When the V_{sheath} is increased, sample stream cross section becomes smaller. V_{sample} is increased, sample stream shape becomes flatten.

The cross section with low sheath flow rate caused the distortion of photon burst histograms because the analyte stream was larger than that of the laser spot as described earlier. Also, there would be high possibility that multiple analytes pass through the detection spot simultaneously. In addition, the flat shaped analyte streams were also observed at the higher sheath flow rate. Although the vertical resolution was improved, the analyte stream was extended to *x*-direction and the width of analyte stream was still larger than laser spot. Moreover, higher flow velocities were avoided due to the limitation of sampling frequency of APD. By considering these two factors, the flow rate was optimized $V_{Analyte}$:V_{Sheath} =1:60 (μl/min) and used for the single molecule photon detections. Then, QD525-antibody in DI water was pumped through the analyte inlet and the laser was focused at the top of the triangular shaped analyte stream.

Figure 12 (a) showed that the photon bursts which were obtained from QD525-antibody sample solution for 10 seconds period (data shown in 20 μs interval). These photon bursts were correlated to obtain auto-correlation curve that was fitted by using non-linear fitting method,[50-52] as shown in Figure 12 (b). The width of analyte stream and effective detection volume were calculated from the correlation curve fitting. The calculated width of analyte was 0.3 μm, and it was smaller than calibrated laser beam diameter (1.1 μm). This result indicated that the analyte flow was completely filled inside the laser beam path. The effective detection volume was estimated as 1.7 nL and this condition was used for all detections (Figure 12 (c)).

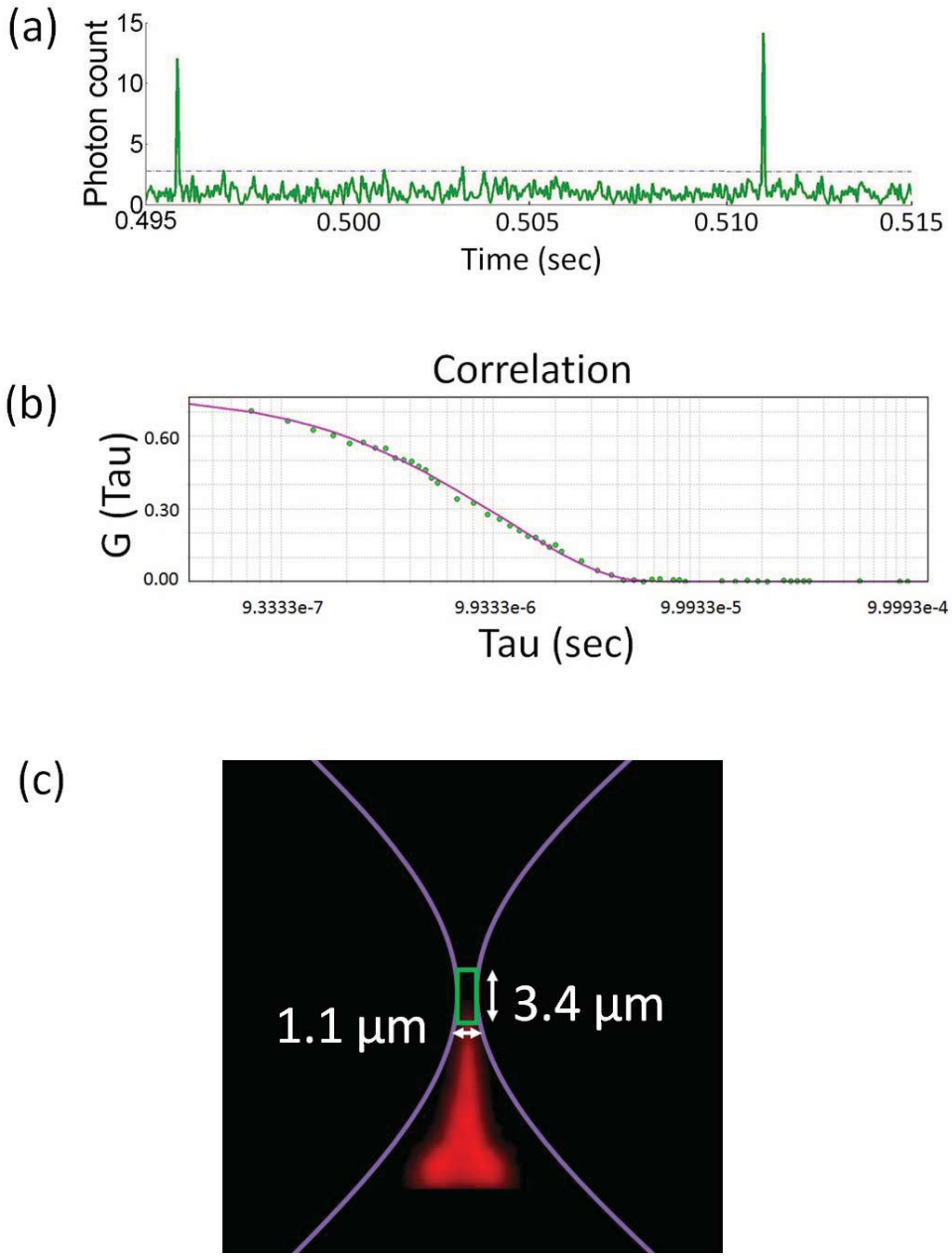

Figure 12. The effective volume of analyte stream. (a) Photon bursts graph as a function of time obtained from QD525 in 20 µs interval. (b) Fluorescent correlation fitting. (c) The effective volume area compared to calibrated laser spot (green square: the calibrated laser spot, white dotted line: the wall of the channel).

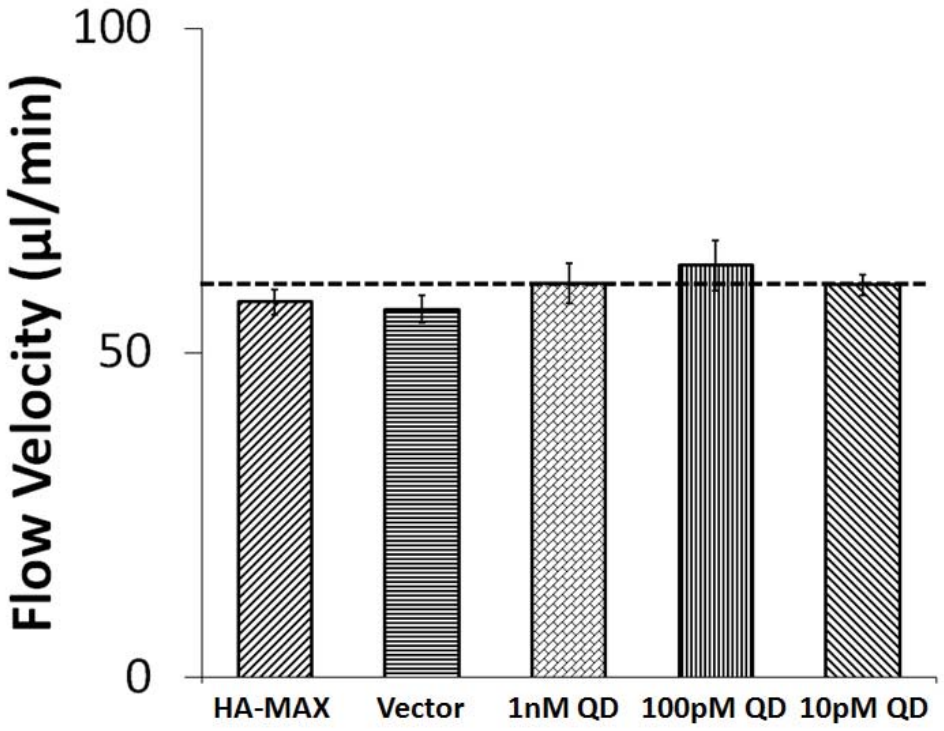

Figure 13. Flow velocity analysis (dotted line: total flow rate setting of syringe pump (61µl/min)).

In order to analyze the stability of the flow, flow velocity data was acquired from photon bursts data of QD525 by Fluorescence Correlation Spectroscopy. Since the detection time was 10 seconds, constant velocities were obtained for all samples as shown in Figure 13.

2.7.2 Quantitative Detection of QD525-antibody

QD525-antibody analyte samples with different concentration were examined using the 3D hydrodynamic flow focusing microfluidic device. The original QD525-antibody solution with 1µM was diluted $1/10^3$ (1nM), $1/10^4$ (100 pM) and $1/10^5$ (10 pM)

times via PBS solution and these three samples were characterized with the flow condition of 1 μl/min ($V_{Analyte}$) and 60 μl/min (V_{Sheath}). Photon bursts for each QD525-antibody concentration were shown in Figure 14 (a), (c) and (e) in 20 μs interval.

It is obvious that more photon bursts were detected by increasing analyte concentrations. After the FFT filtering with 1 μs bin time, photon counts were normalized by 100 counts to 1.0. The histogram of normalized photon bursts were plotted as shown in Figure 14 (b), (d) and (f). The 1 μs bin time was determined by analyte residual time calculated from how long it took for analyte to pass through the detection volume. In these histograms, there were two distribution peaks. Because the first peaks showed Poisson distribution, these were defined as noise distributions from detection equipment and background. The second peaks in the histograms were defined as single molecule signals from QD525-antibodys due to their Gaussian distribution. In this histogram, the positions of secondary peaks were shifted because the background noise levels increased as following QD525-antibody concentration increase.

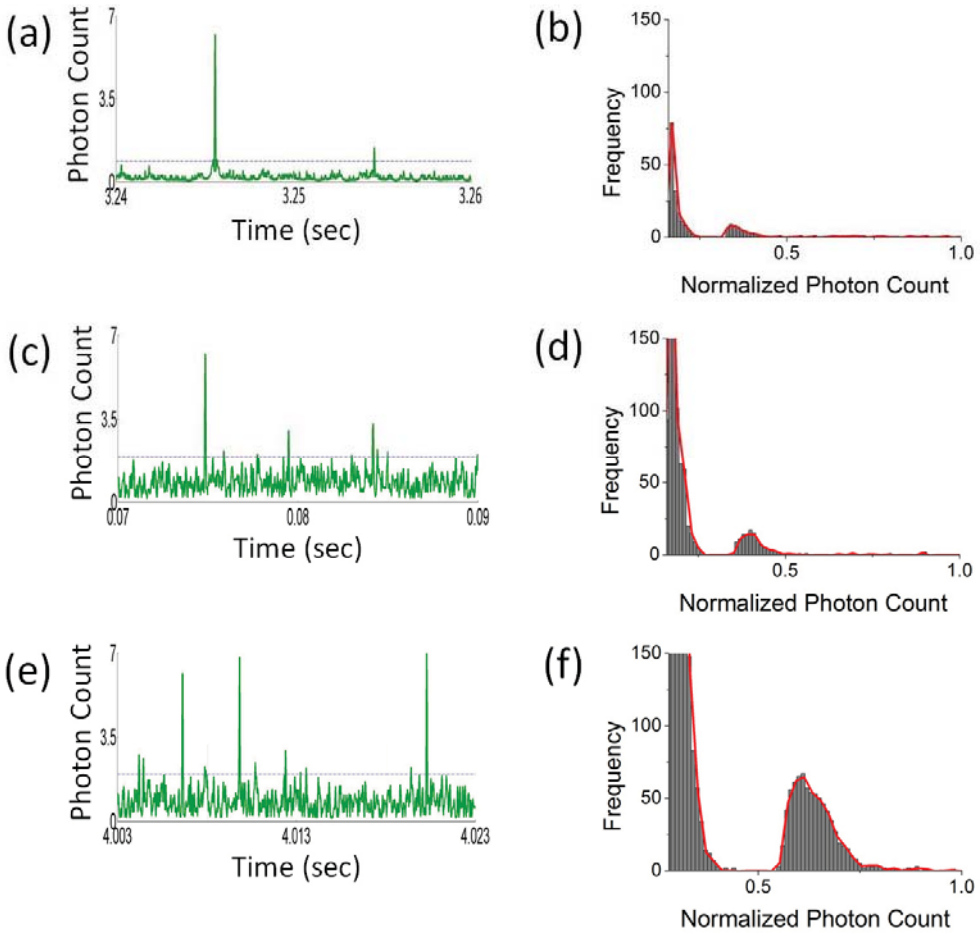

Figure 14. QD detection with different concentration. (a) Photon burst signal of QD at 10 pM in 20 μs interval. (b) Histogram of QD at 10 pM. (c) Photon burst signal of QD at 100 pM in 20 μs interval. (d) Histogram of QD at 100 pM. (e) Photon burst signal of QD at 1 nM in 20 μs interval (f) Histogram of QD at 1 nM.

The numbers of QD525-antibodys in the second peaks were counted and averaged for each result, then plotted as bar graphs with standard deviation as shown in Figure 15. It clearly showed that the numbers of detected QD525s were linearly increased with small standard deviation. Based on detected numbers of QD525-antibody, detection volume, and flow rate, the concentrations of QD525-antibody were calculated as 0.971 ± 0.024 nM, 131 ± 40 pM and 11 ± 5 pM for 1nM, 100pM and 10pM QD525-antibody solutions, respectively. These results indicate that our system works properly to determine the protein concentrations since the calculated concentrations from obtained data are closed to original concentrations.

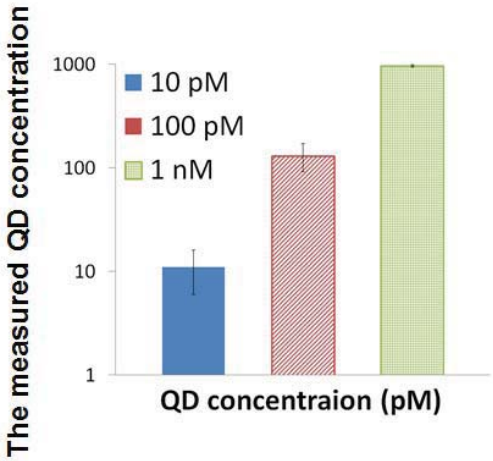

	QD concentration (pM)		
Original	10	100	1000
Measured	11±5	131±40	971±24

Figure 15. The quantified graph of the number of detected QD with different concentrations and summary of the measured QD concentrations.

2.7.3 Quantitative Detection of HA-MAX

Subsequently, the concentration of HA-MAX proteins in cell lysate solutions was also determined. 1 nM QD525-antibodies were hybridized to anti-HA rabbit polyclonal antibody specifically binds to HA tag of HA-MAX proteins. Thus, QD525-conjugated rabbit IgG secondary antibody recognize HA-MAX by binding anti-HA antibody. As a result, multiple QD525s could bind to HA-MAX proteins. As a first step, HEK293 cells without HA-MAX expression were lysed and characterized as a control. In this sample, there was no HA-MAX protein available for anti-HA antibody to recognize. Cell lysate solution mixed with QD525s-conjuated secondary antibody and PBS solution were pumped through the analyte and sheath inlets, respectively. Photon bursts for each sample were detected 5 times for 10 seconds. The typical photon bursts obtained from the control sample was shown in Figure 16 (a) in 20 μs interval. These peaks were from single QD525-antibodies and the photon burst histogram was plotted as shown in Figure 16 (b). This histogram showed similar distribution compared to the one in Figure 15 (f) that contained a single Gaussian distribution. The number of detected QD525-antibodies in the Gaussian distribution was 958. HA-MAX expressed HEK293 lysate were hybridized with anti-HA-antibody and QD525s-conjugated secondary antibody for labeling. Figure 16 (c) showed the photon bursts of the HA-MAX expressed sample as a function of time (in 20 μs interval). Obviously, there was the photon burst that had higher photon counts than those in Figure 16 (a) because HA-MAX protein carried more than single QD525s. Individual photon bursts were plotted in the photon burst histogram as shown in Figure 16 (d). In this histogram, two obvious Gaussian peaks were obtained.

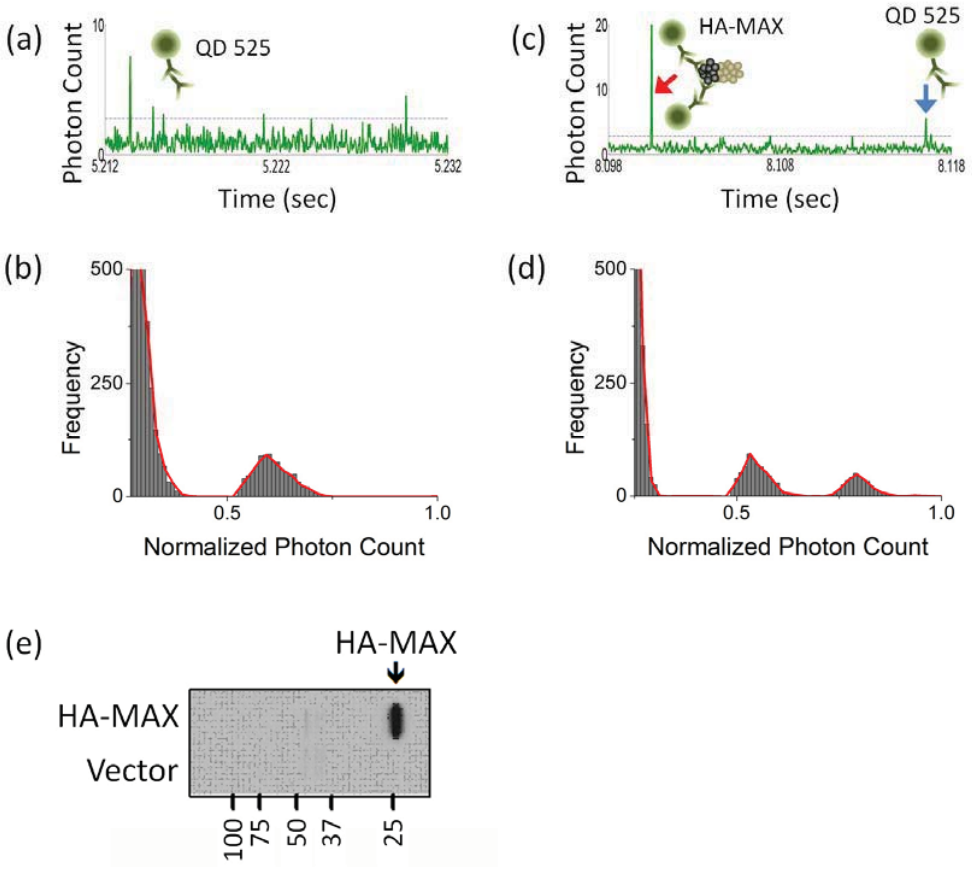

Figure 16. Results of HA-MAX detection. (a) Photon burst signal profile of vector in 20 μs interval. (b) Histogram of Vector. (c) Photon burst signal profile of HA-MAX in 20 μs interval. (d) Histogram of HA-MAX. (e) Western blot result of the same samples.

The first Gaussian peak was concluded as unbound QD525-antibodies as proven in Figure 16 (b) and Figure 15. The second peak concluded as HA-MAX protein because HA-MAX protein had more than one QD525s. In this histogram, numbers of HA-MAX and unbound QD525 were counted as 347 and 674, respectively. The concentration of HA-MAX was determined as 0.283 ± 0.015 nM by considering detected events, detection volume, and flow rate. This process only requires for 1 minute. The expression of HA-MAX was also characterized by the conventional western blot, which required for 24 hours of biochemical processes, as shown in Figure 16 (e). From the result of western blot, HA-MAX expression could be observed, but it did not provide quantitative information of HA-MAX concentration.

3. MEASUREMENT OF P-53 DIFFUSION USING RICS

3.1 Introduction

Analysis of protein-protein or protein-DNA interaction is indispensable for current molecular biology to understand various signaling pathways that are essential for maintenance of cellular functions in living cells. To this end, several biochemical and molecular biological techniques have been developed, such as far western blot,[53] co-immunoprecipitation,[54] Mass spectrometry,[55] electromobility shift assay (EMSA),[56] and chromatin immunoprecipitation (ChIP).[57] Although these techniques have their own advantages, they require long process time and a large amount of samples. More importantly, these techniques do not provide the information regarding the high spatial and temporal interaction dynamics that may provide the novel insight into current biology. Thus, several techniques, for example, Single Particle Tracking (SPT),[58] Fluorescence Recovery after Photo bleaching (FRAT),[59] and Foster Resonance Energy Transfer (FRET),[60, 61] have been developed to provide higher temporal/spatial resolution for molecular dynamics in living cells. Recently, Digman and co-workers introduced the new approach, called as Raster Image Correlation Spectroscopy (RICS), which enables to measure the protein dynamics in a living cell by using commercial laser scanning confocal microscope without adding additional expensive components. The detailed theories are described elsewhere.[62-65]

The tumor-suppressor protein p53, that has been known as “the guardian of the genome,” is frequently mutated or deleted in variety of human cancer types and plays an essential role in tumorigenesis.[66] In response to DNA damage, p53 is phosphorylated at several serine/threonine residues, resulting in its stabilization and activation.[67] Activated p53 forms a complex with multiple transcription co-factors and binds to promoter regions of target genes such as p21, Bax GADD45 and Puma that are involved in cell cycle arrest or apoptosis.[68, 69] Cisplatin and etoposide are DNA damaging agents that have been used as chemotherapeutic drugs. Cisplatin unwind intra- and interstrand crosslinking of DNA while etoposide disrupts DNA replication and repair by inhibiting topoisomerase II enzyme.[70, 71] Thus, both anti-cancer agents damage to DNA that induce p53 accumulation and activation.

3.2 Cell Culture and Drug Treatment

Human cervical cancer, HeLa cells were obtained from American Type Culture Collection (ATCC) and maintained in DMEM/F12 medium supplemented with 10 % fetal bovine serum and antibiotics. pEGFP-C2 was obtained from Clontech laboratories. p53 Open Reading Frame was digested out from pcDNA3-myc-p53 with EcoRI and XhoI, and ligated into pEGFP-C2 EcoRI/SalI sites. pcDNA3-myc-p53 was prepared by polymerase chain reaction (PCR) and described previously.[72] EGFP empty vector or GFP-p53 expression plasmid was transfected into HeLa cells using electroporation. After 24 hours transfection, the cells were seeded in 50 mm Glass Bottom culture dish (MatTek Corp.) at around 50 % density and cultured for additional 12 hours. Since our

preliminary experiments showed that over 50 μM drugs induced apoptotic cell death after 24 hours, the cell samples were treated or untreated with either 20 μM cisplatin (Sigma) or 20 μM etoposide (Sigma) for the different periods of time and subjected to confocal microscopy analysis.

3.3 Confocal Microscope Setting

The confocal fluorescent microscopy (Olympus FV100) equipped with air-cooled 488nm argon ion laser was employed for this study (Figure 17). The series of images were collected using 60X water immersion objective (NA=1.2). The scan speed was set at 12.5 μs/pixel. The scan area was 256 × 256 pixels and 100 frames were collected for each sample. The corresponding line and the frame time were 4.325 ms and 1.150 s, respectively. 488 nm wavelength of laser with 1.5 % power was used for the GFP excitation, and emission spectrum was filtered between 500 and 600 nm. The microscope was operated in the pseudo photon counting mode. The beam waist radius was calibrated using 10 nM fluorescein in 0.01M NaOH at the beginning of experiment, and it was 0.5 μm. The collected fluorescence data were analyzed using the Globals software package developed at the Laboratory for Fluorescence Dynamics at the University of California at Irvine.[73]

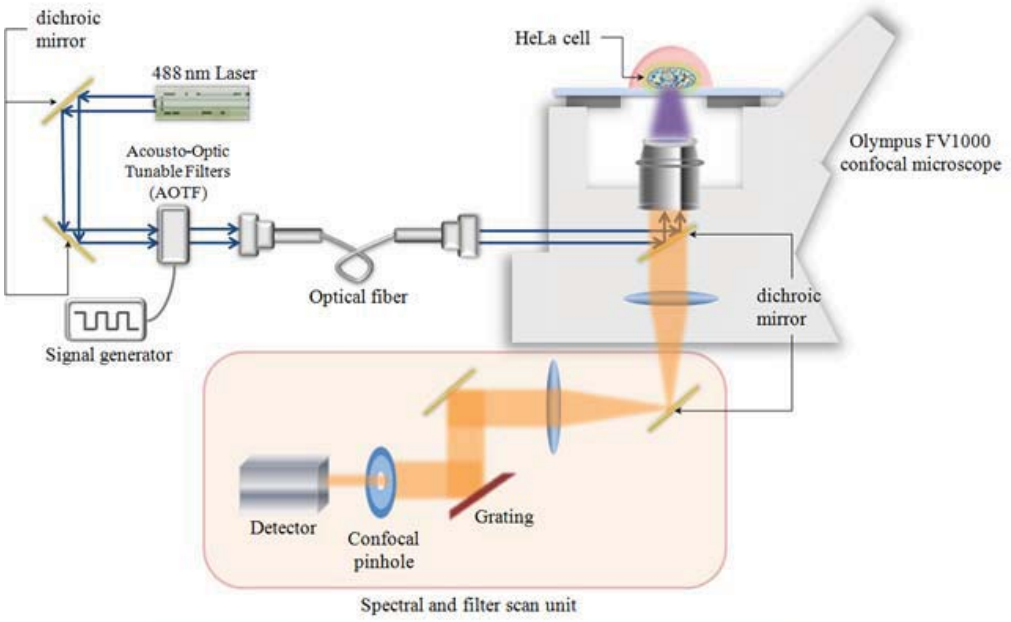

Figure 17. Schematic diagram of system setting.

3.4 Results and Discussion

3.4.1 GFP Diffusion Dynamics Analysis

Figure 18 showed the RICS analysis for GFP alone in living HeLa cells immediately after adding cisplatin and etoposide. The diffusion coefficients were measured every 4 hours after adding the drugs. The GFP samples were used to calibrate the RICS analysis. The autocorrelation spectrum after background subtraction showed that GFP diffused freely into the nucleus. The measured diffusion coefficients of GFP were 38.26 ± 5.62 $\mu m^2/s$ (cistplatin-treated) and 41.32 ± 9.81 $\mu m^2/s$ (etoposide-treated) at the 0 hour. Also, consistent values were observed over time (43.73 ± 6.57 $\mu m^2/s$ and 44.36 ± 6.82 $\mu m^2/s$ at the 16 hour) as shown in Table 2.

Table 2. Summary of GFP diffusion coefficient in the nuleus of HeLa cells

	Diffusion Coefficient ($\mu m^2/s$)				
	0 hr	4 hr	8 hr	12 hr	16 hr
Etoposide	41.32±9.81	36.54±6.61	41.21±8.29	44.72±8.97	44.36±6.82
Cisplatin	38.26±5.62	37.55±5.67	42.65±9.46	44.72±9.14	43.73±6.57

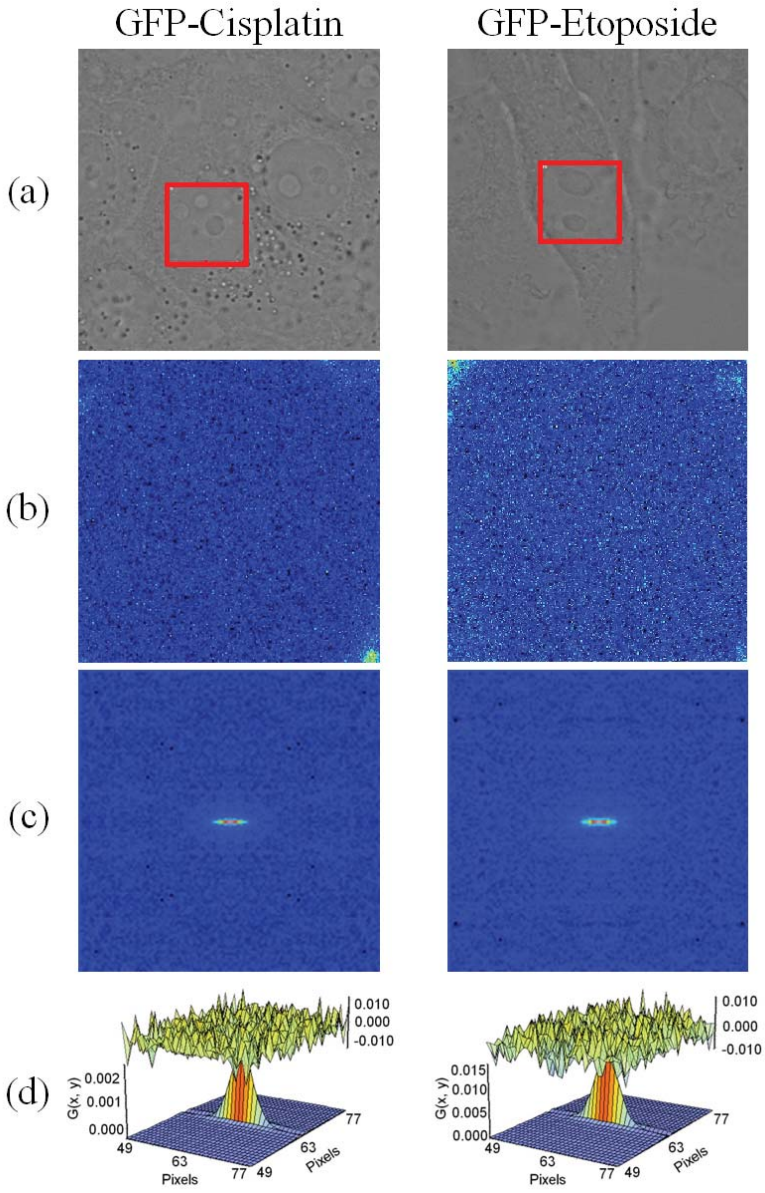

Figure 18. RICS analysis of GFP in live HeLa cells at after anti-cancer drugs treatment. (a) Optical images of HeLa cell with the region of interest (ROI) for RICS analysis, (b) intensity images of ROI (nucleus), (c) RICS autocorrelation function of 128×128 pixels, (d) fit (lower surface) and residues (upper surface) of the spatial correlation function.

To compare the dynamics of p53 in response to DNA damaging agents, HeLa cells expressing GFP-tagged p53 were exposed to cisplatin or etoposide and subjected to RICS analysis. We first collected 100 frame images of GFP-p53 immediately after drugs treatment. Following, GFP-p53 in HeLa cells treated with the drugs were monitored every 4 hours upto 16 hours.

3.4.2 GFP-P53 Diffusion Dynamics Analysis

Figure 19 showed the auto-correlation of confocal images and fitting of the spatial correlation function at 16 hours after drugs treatment. These results suggest that GFP-p53 interacts with other molecules such as proteins and DNAs after the drug treatment and, as a result, the diffusion coefficients were reduced. The diffusion dynamics changes of GFP-p53 in response to the drugs were summarized in Table 3.

Table 3. Summary of GFP-p53 diffusion coefficient in the nuleus of HeLa cells

	Diffusion Coefficient ($\mu m^2/s$)				
	0 hr	4 hr	8 hr	12 hr	16 hr
Etoposide	18.76±2.68	12.77±5.42	3.05±0.60	3.57±1.08	3.25±1.36
Cisplatin	19.92±3.64	8.23±5.78	3.25±0.38	3.21±1.18	3.28±2.87

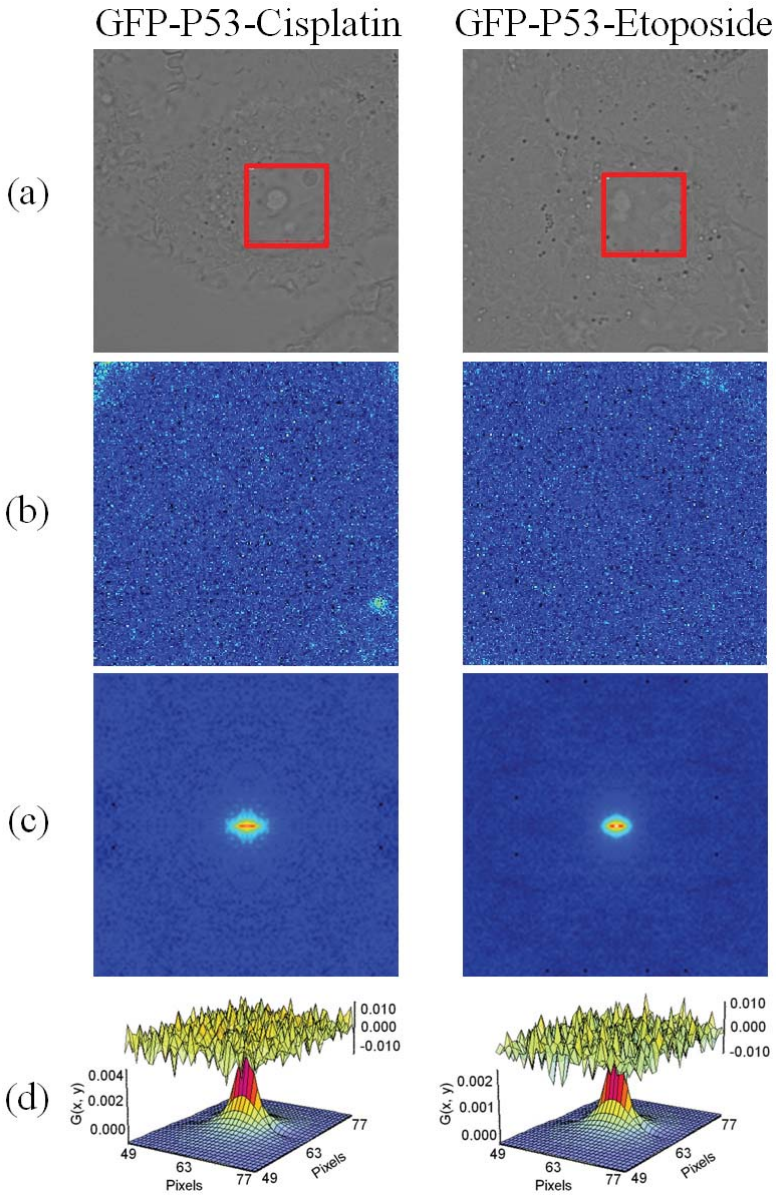

Figure 19. RICS analysis of GFP-p53 in live HeLa cells at 16 hours after anti-cancer drugs treatment. (a) optical images of HeLa cell with the region of interest (ROI) for RICS analysis, (b) intensity images of ROI (nucleus), (c) RICS autocorrelation function of 128×128 pixels, (d) fit (lower surface) and residues (upper surface) of the spatial correlation function.

As shown in Figure 20, the measured diffusion coefficients of GFP-p53 were 19.92 ± 3.64 $\mu m^2/s$ and 18.76 ± 2.68 $\mu m^2/s$ immediately after adding cisplatin and etoposide, repectively, and these results were in a good agreement with previous reported result (15.4 ± 5.6 $\mu m^2/s$) [74]. The diffusion dynamics of GFP-p53 were gradually decreased over time, and significant reductions of GFP-p53 mobility were observed at 8 hr after drugs injection, (3.25 ± 0.38 $\mu m^2/s$ for cisplatin and 3.05 ± 0.60 $\mu m^2/s$ for etoposide).Then, it maintained the constant values after 8 hr in the presence of both drugs.

In this work, we measured the diffusion coefficient of GFP-tagged p53 in the nucleus of HeLa cells using RICS approach. Also, DNA damaging agents were used to verify p53 dynamics in response to DNA damage. The diffusion coefficients of GFP obtained by RICS were agreed well with previously reported value. Hinow et al. applied free diffusion model to explain the mobility of GFP in the nucleus of H1299 human large cell lung carcinoma cell using confocal FRAP technique, and they reported the diffusion coefficient of GFP (41.6 ± 13.6 $\mu m^2/s$).[75]

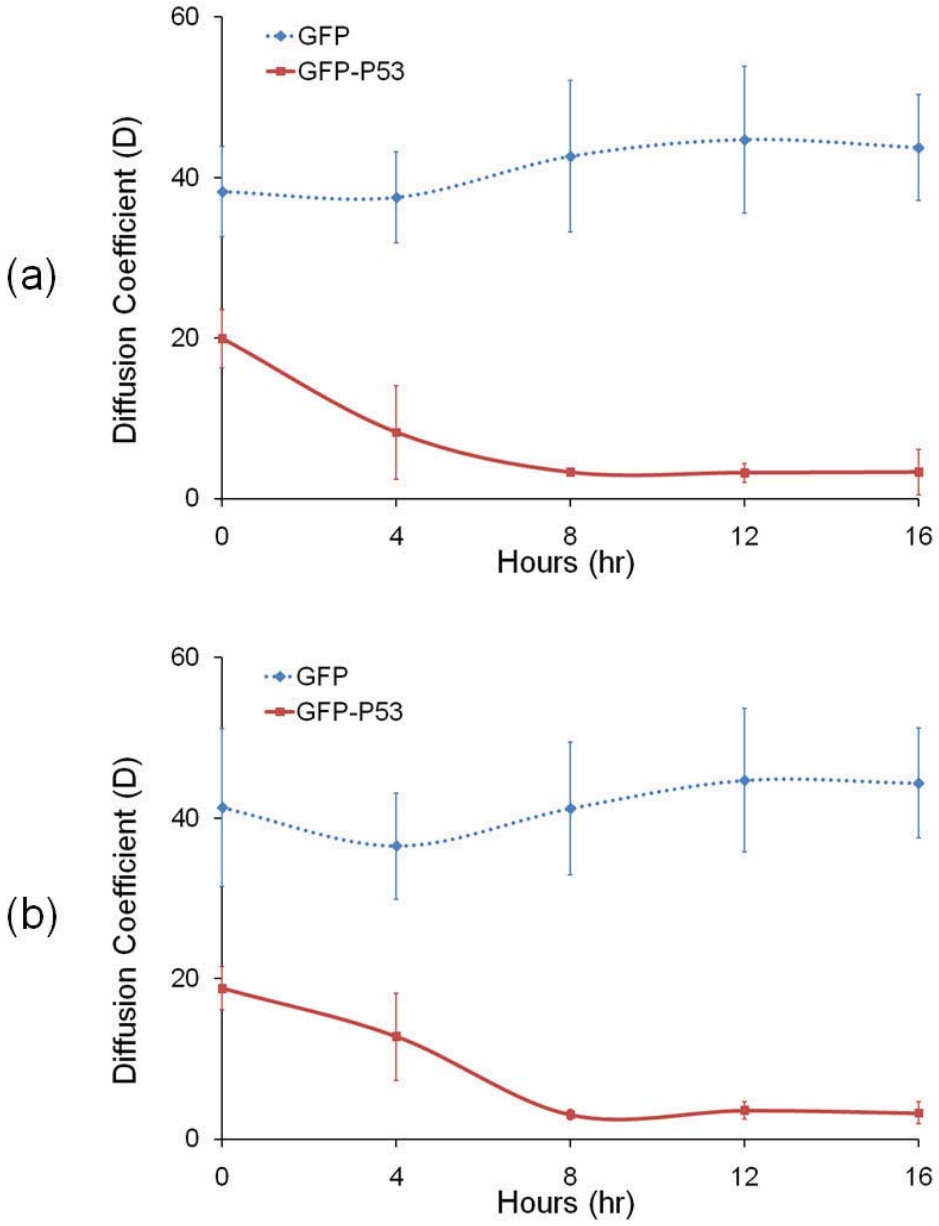

Figure 20. The diffusion coefficient graph as a function of time. (a) diffusion dynamics changes of GFP or GFP-p53 in cisplatin treated cells, (b) diffusion dynamics changes of GFP or GFP-p53 in etoposide treated cells.

Since GFP was not involved in DNA damage response, the diffusion of GFP was not affected by anti-cancer drugs. This demonstrated that RICS method could provide the stable result in measuring diffusion coefficient in living HeLa cells. After DNA damaging agent treatment, the significant reductions in GFP-p53 mobility were observed in the nucleus. It is well known that p53 is stabilized and activated in response to DNA damage.[76] In this study, 20 μM concentrations of cisplatin and etoposide were used. It would be expected that higher concentration of drugs induces the quicker reduction of the mobility of GFP-p53 due to the p53 activation by more DNA damage. Furthermore, it has been known that ciplatin induces single stranded break of DNA[77] while etopside causes double stranded break of DNA.[78] Thus, the combination of these drugs induces more DNA damage, and it also would be expected that the combination of both drugs induces the quicker reduction of the mobility of GFP-p53.

Moreover, it has been shown that p53 translocates from cytosol to the nucleus after DNA damage. Activated p53 form a complex with multiple transcriptions co-factors and binds to the specific promoter region in DNA to induce target genes within 8 hours. As a result, p53 mobility was expected to be decreased. Our results for fluctuations of GFP-p53 diffusion coefficients were consistent with our prediction from the current knowledge regarding p53.

4. MICROFLUIDIC INTEGRATED PLATFORM

4.1 Introduction

Cell-containing microspheres are widely used as building blocks in many biomedical applications such as tissue engineering,[79-82] cell-based biosensors,[83-85] and encapsulated cell delivery.[86-88] These applications require uniform microsphere dimensions and morphology with high cell viability. Live cells are typically encapsulated in biodegradable polymers such as alginate,[89, 90] polyethylene glycol (PEG),[91] and collagen[92, 93] that are highly porous, allowing adequate transport of nutrients and oxygen to the cells. Collagen is a particularly attractive material for microspheres as it is the most abundant scaffold protein in tissues[94] and contains specific cell-binding sites that contribute to normal cell function.[95]

Collagen microspheres are commonly generated by first forming microdroplets of cells in collagen via direct aliquoting or via emulsification, and subsequently microspheres are formed via gelation of the collagen. Currently, there is no report regarding the generation of collagen microspheres in microfluidic devices. Aliquoting involves dispensing small volumes (a few microliters) of aqueous collagen solution onto a surface.[87, 96-98] In emulsification, aqueous collagen solution is dispersed into microdroplets within a continuous oil phase solution.[99, 100] The emulsified microspheres are then typically separated from the oil phase by centrifugation.[101] These conventional approaches are tedious, requiring that each step (*i.e.* droplet generation, gelation, and extraction) be performed separately. Another drawback of these techniques is the difficulty in maintaining uniform microsphere dimensions and shapes at a high

production rate. Recently, an axisymmetric flow-focusing device (AFFD) was developed[102] to generate collagen microspheres. The mono-dispersed collagen microdroplets were generated at the orifice of a nozzle in the AFFD and collected in a test tube. The collected collagen microdroplets were gelled at 37°C for 45 min. Due to the forces generated during centrifugal extraction, the dimensions and shapes of the resulting collagen microspheres were non-uniform due to coalescence of microdroplets. In addition, low cell viability was observed that was attributed to the centrifugation process.[101] The bioprinting platform also produced cell encapsulated collagen droplets.[103] This approach enables multilayered 3D cell-laden hydrogel structures, high-throughput droplet generation, and long-term viability; however, the shapes of collagen droplets would not be spherical due to gravity.

4.2 Droplet Generation Techniques

4.2.1 T-junction Geometry

T-junction structure is the most widely used for the droplet generation because it has the simplest geometry and mechanism.[104, 105] As shown in Figure 21, droplets are generated by shear force of a continuous flow (normally used oil), which is connected perpendicularly to disperse phase (normally water). The disperse flow was cut off by vicious drag force of the continuous flow and generate droplets. The size of the droplets are able to control by the flow rate changes and the channel dimensions.

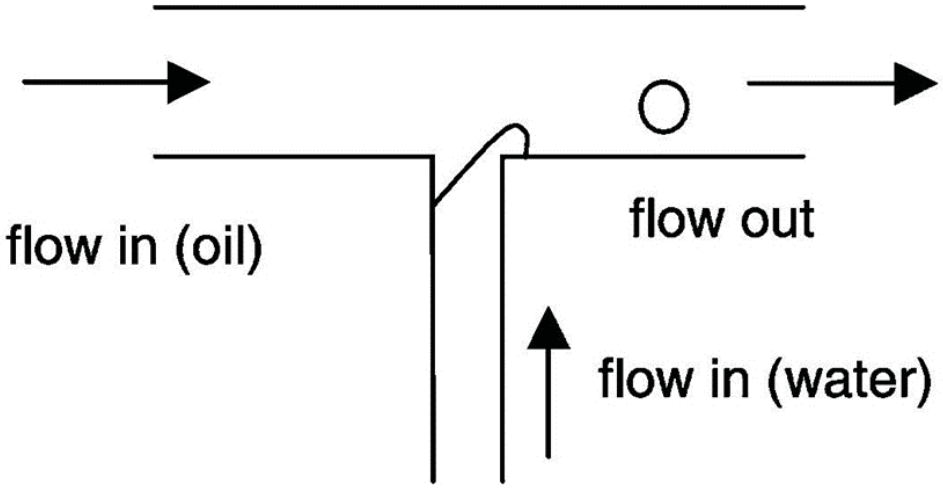

Figure 21. The principle of droplet formation at a T-junction.[105]

4.2.2 Hydrodynamic Flow Focusing

Another method for droplet generation is a hydrodynamic flow focusing.[106-108] A hydrodynamic flow focusing device has two side channels which contain continuous phase and a main channel contains dispersed phase. The continuous phases from side channels are forced aqueous dispersed phase to flow to the narrow orifice and the dispersed phase breaks off by pressure and viscous stresses (Figure 22). Similarly, the droplet size is adjustable by flow rate control, channel dimension, and orifice size.

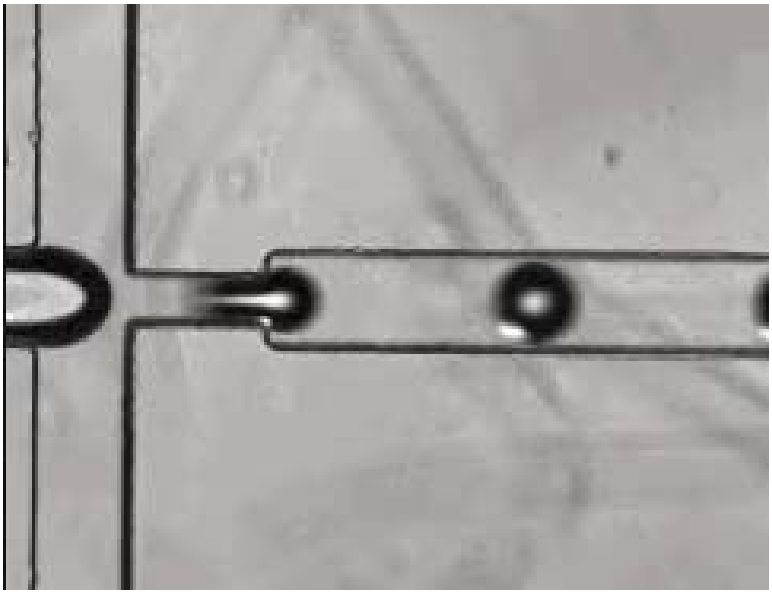

Figure 22. Basic flow focusing setup with a disperse phase and a continuous phase.

4.3 Device Fabrication

Microfluidic devices were fabricated on poly (dimethylsiloxane) substrate (PDMS; Dow Corning, Midland, MI) by standard micro-molding procedures.[48, 110, 111] Two lithographic processes fabricated a master mold of a microfluidic chip on a silicon wafer. First, SU-8 2075 photoresist (Microchem Corp., Newton, MA) was spin-coated with thickness of 100 μm on a silicon wafer. Shallow microchannels for microsphere extractions were defined by a contact aligner. As the second lithographic process, a SU-8 2075 layer of 300 μm thickness was spin-coated on top of the shallow channel-patterned silicon surface and defined as a deep main channel that was directly connected to the shallow channels to form a step junction structure. The top channel master mold was also fabricated, which contained the pre-warmed mineral oil injection port. As the final

step, uncured PDMS polymer solution was dispensed over the lithographically patterned silicon molds and cured at 65 C° for 2 hours. The microfluidic chip consists of three layers of PDMS substrate. The top PDMS layer contains the pre-warmed mineral oil delivery port and an extraction chamber. The main channel structure is located in the second PDMS layer, and third layer contains the collagen microsphere extraction chamber (Figure 23). These three PDMS layers and a bottom glass substrate (170 μm thickness) were bonded after oxygen plasma treatment.

4.4 Preparation of Collagen-MDA 231 Mixture

The human breast cancer cell line MDA-MB-231 expressing Green Fluorescent Protein (GFP) was cultured in Dulbecco's Minimal Essential Medium (DMEM)/F12 medium supplemented with 10% fetal bovine serum (FBS). Cells were cultured in a humidified 5% CO_2/95% air incubator at 37°C. Cells were removed with trypsin-EDTA from the culture dish and centrifuged. A 1×10^8 cells/ml concentration of MDA 231 cells was suspended in rat tail collagen type 1 solution at a concentration of 3.5 mg/ml as previously described.[112-114]

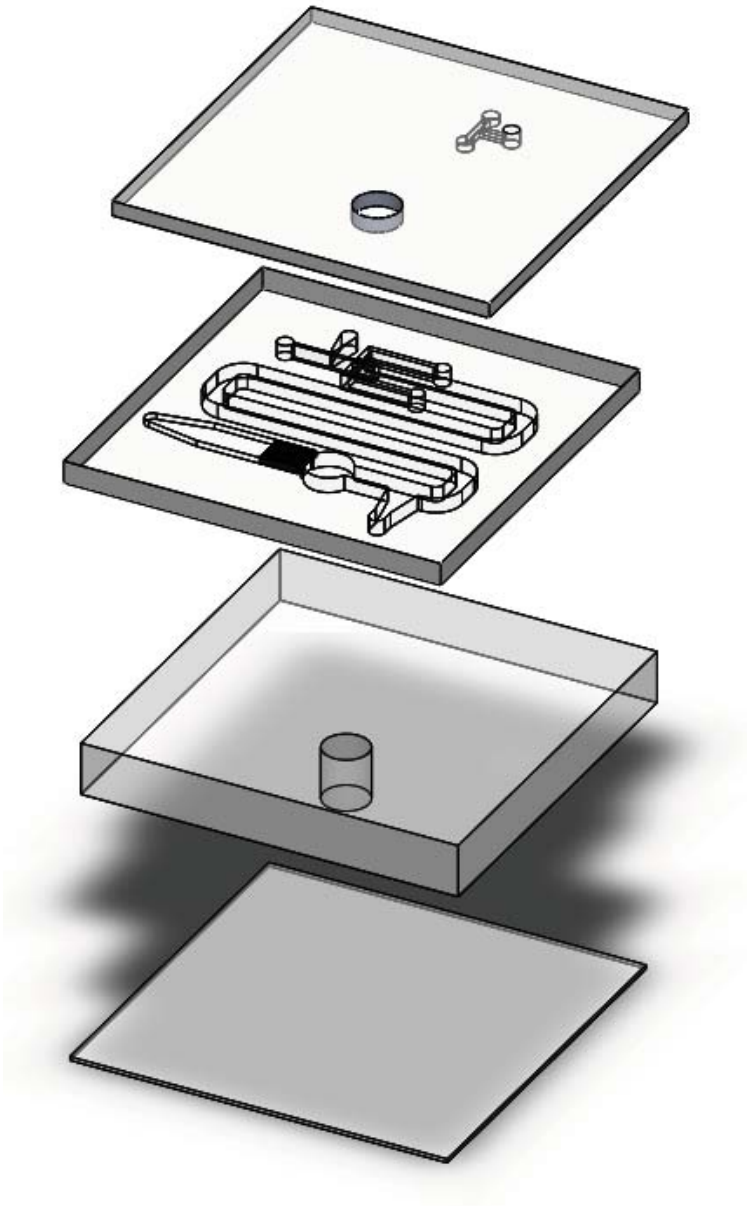

Figure 23. The configuration of the microfluidic platform consisting of three PDMS and one glass substrates, all of which are bonded.

4.5 Coaxial Cooling System

In order to maintain collagen temperature below 4°C to avoid premature collagen gelation, coaxial cooling system was applied as shown in Figure 24. 1mL syringe was surrounded by plastic tubing which contained frozen refrigerant gel, and connected to cylindrical coaxial cooling tube. Metal tubing was placed in the center of cooling tube and larger plastic tubing was covered on metal tubing. It also had refrigerant gel inside of plastic tubing and was kept in the -20°C refrigerator before using this system. By using this cooling system, collagen was able to deliver to microfluidic platform over 1hour without collagen gelation.

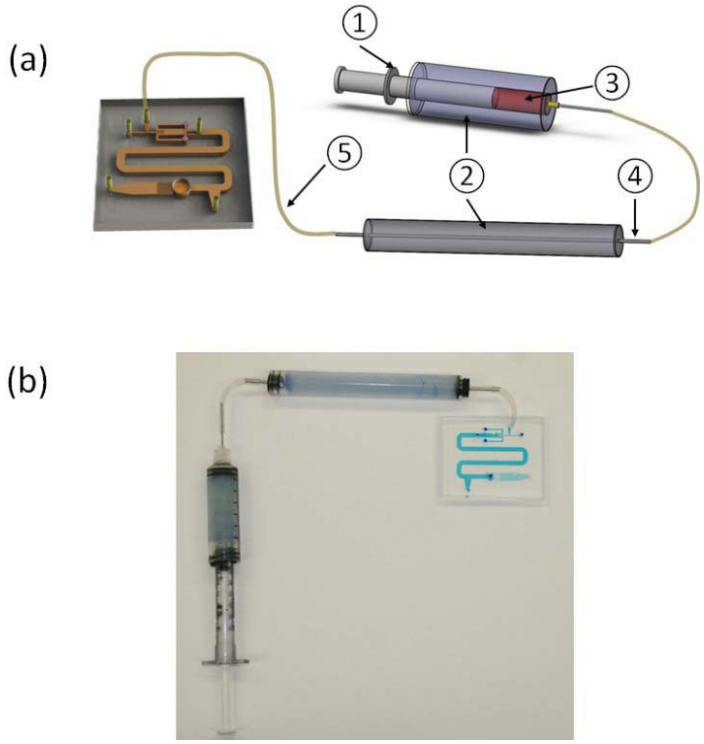

Figure 24. Coaxial cooling system. (a) The schematic diagram: 1. 1mL syringe, 2. refrigerant gel, 3. collagen solution, 4. metal tubing, and 5. tygon tube. (b) photography of cooling system.

4.6 Collagen Microspheres Formation

A schematic diagram and photograph of the microfluidic platform are shown in Figure 25 (a) and (b), respectively. The pre-mixture of collagen and cell solution was delivered via the collagen injection port as shown in Figure 25. The temperature of the collagen solution was maintained below 4ºC using coaxial cooling tubing, allowing stable pumping of the collagen solution by avoiding premature collagen gelation for more than 1 hour.

Collagen solution and cold mineral oil were injected with two separate syringe pumps (11 plus, Harvard Apparatus, Cambridge, MA). A 2% concentration of Span 80 (surfactant) was added to the mineral oil to facilitate droplet stabilization. At the T junction, shear forces from the mineral oil flow periodically separated the collagen flow into discrete collagen microdroplets. The two-phase flow was blended with pre-warmed mineral oil (40°C) in the gelation channel through interconnection holes. The relatively wide gelation channel (2 mm) allowed collagen microdroplets to spontaneously form spherical shapes by minimizing aqueous-oil phase surface interactions. Collagen microspheres continuously flowed through the gelation chamber to prevent adhesion to the walls and collected in a deep extraction chamber containing a filter gate.

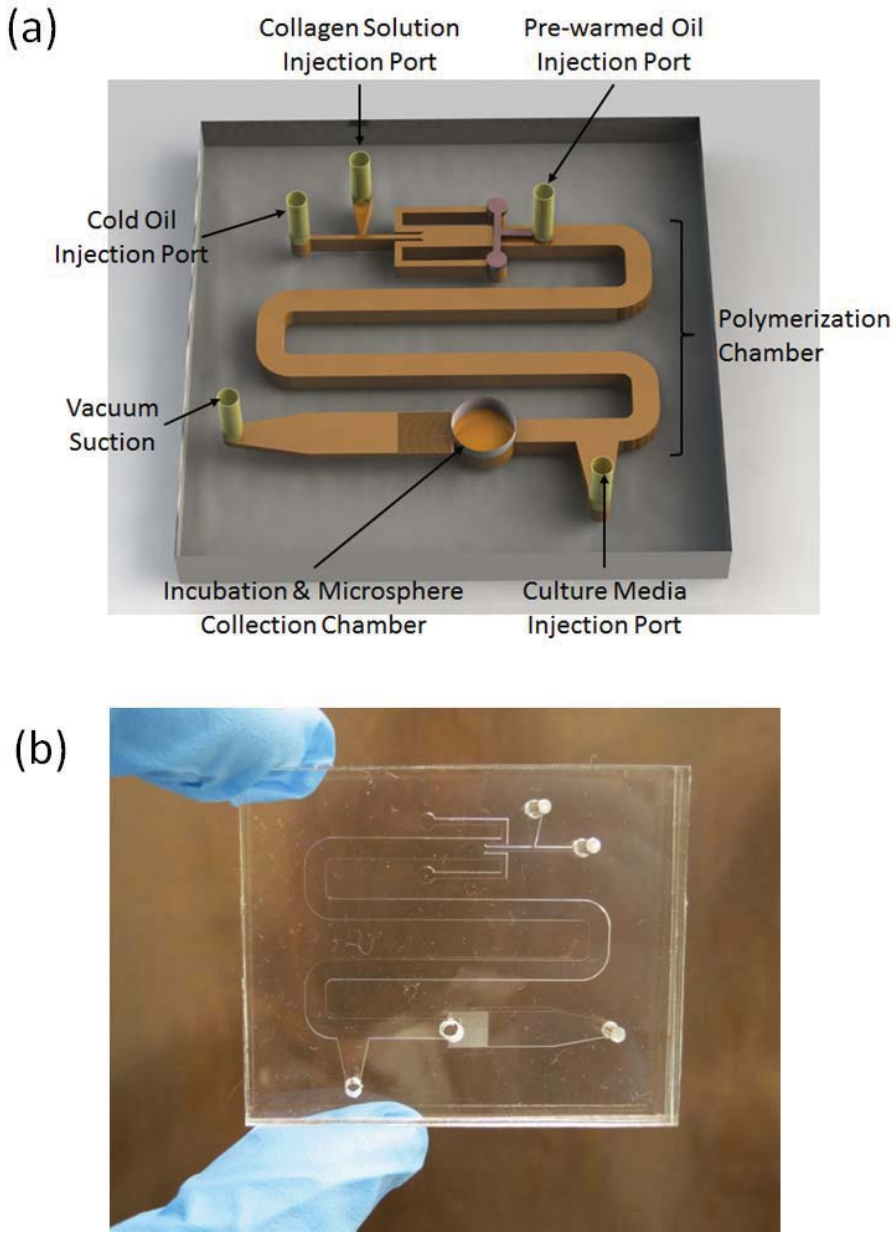

Figure 25. The design of the microfluidic chip. (a) The schematic diagram of microfluidic chip that contained three functional channels: droplet generation, gelation and extraction. (b) Actual photo of a PDMS chip.

Once all collagen microspheres were collected, mineral oil flow was terminated and culture media (indicated by pink color in Figure 26 (a)) was injected through a local injection port to remove mineral oil from collagen microspheres. The rotary pump connected to the extraction chamber continuously sucked solution from the chamber and culture media was continuously pumped in to wash any remaining mineral oil on the surface of collagen microspheres for 3 minutes. The filter gate consisted of multiple microchannels with 100 um width and depth that were smaller than the diameter of the microspheres (Figure 26 (b)). Microspheres were collected from the chip using a micropipette after all flows were terminated. The extracted microspheres were transported to sterile culture dishes and incubated at 37°C in a humidified 5% CO_2 incubator. Our approach provides straightforward and high throughput generation of uniform collagen microspheres encapsulating cells with high viability.

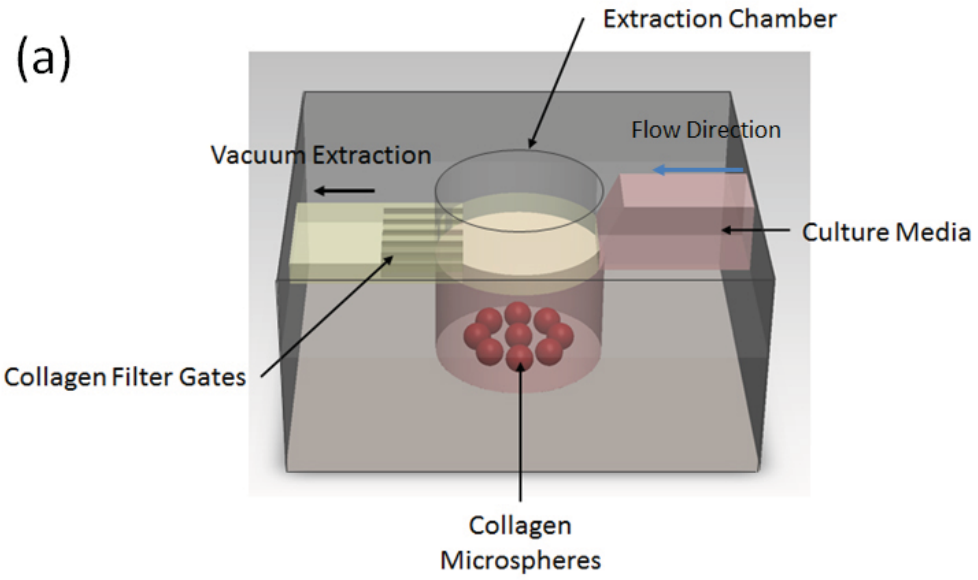

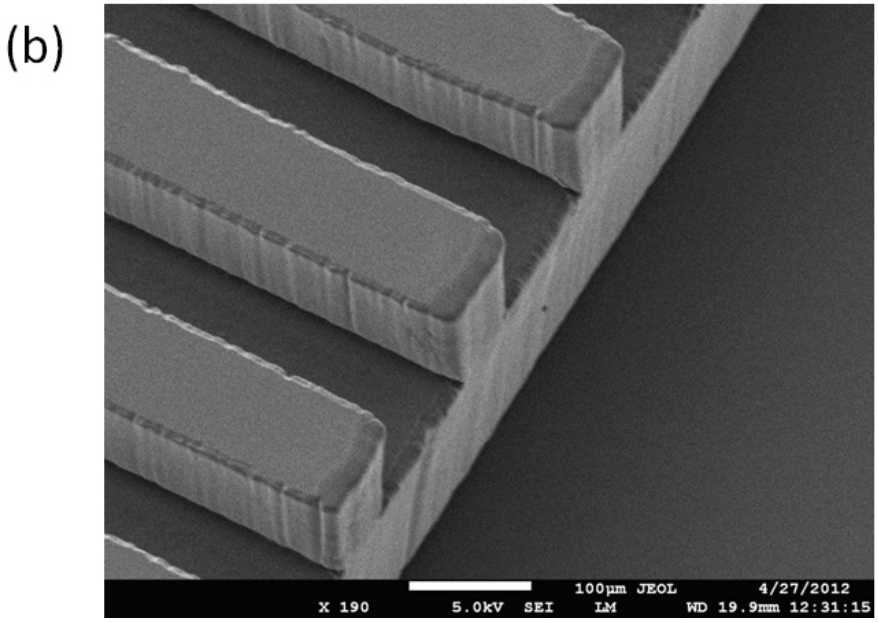

Figure 26. The design of the extraction chamber. (a) The extraction chamber (close-up view) (b) The SEM image of filter gates.

4.7 Collagen Microspheres Extraction System

The detailed schematic diagram for the extraction of collagen microspheres from oil phase is shown in Figure 27. Collagen microspheres are collected in the extraction chamber and incubated until the completion of droplet generations. After termination of droplet generations, culture media was pumped through the injection port. Culture media is filled from the bottom of the extraction chamber due to heavier density. The mineral oil is pimped to the top and sucked to the left side of chamber by the vacuum pump. Finally, all oil phase is replaced to aqueous media (culture media) and microspheres are collected by pipette.

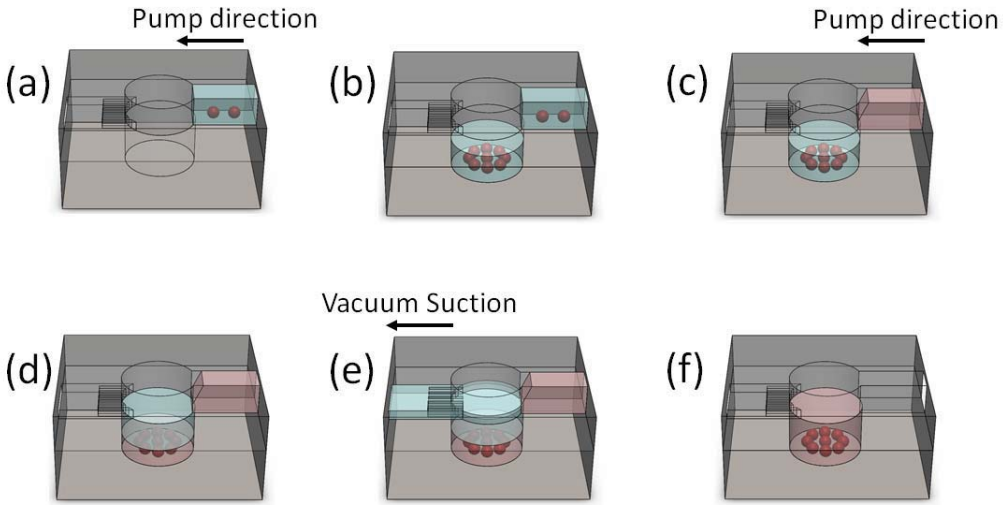

Figure 27. Collagen microspheres extraction. (a) Collagen microdroplets were generated. (b) Microspheres were collected in extraction chamber. (c) Culture media was injected. (d) Mineral oil separation by density. (e) Mineral oil removing by vacuum suction. (f) Collagen microspheres in extraction chamber.

4.8 Overall System Setup

The microfluidic platform was placed on the Nikon Eclipse T*i*-U Inverted microscope stage as shown in Figure 28. Four individual syringe pumps were used to deliver mineral oil, collagen solution, pre-warmed mineral oil, and culture media. Also, rotary pump was used for mineral oil extraction. Fluorescence light (lumen 200) was focused through the objective lens at the observation spot of droplet generation area. All images were recorded by emccd and microscope software.

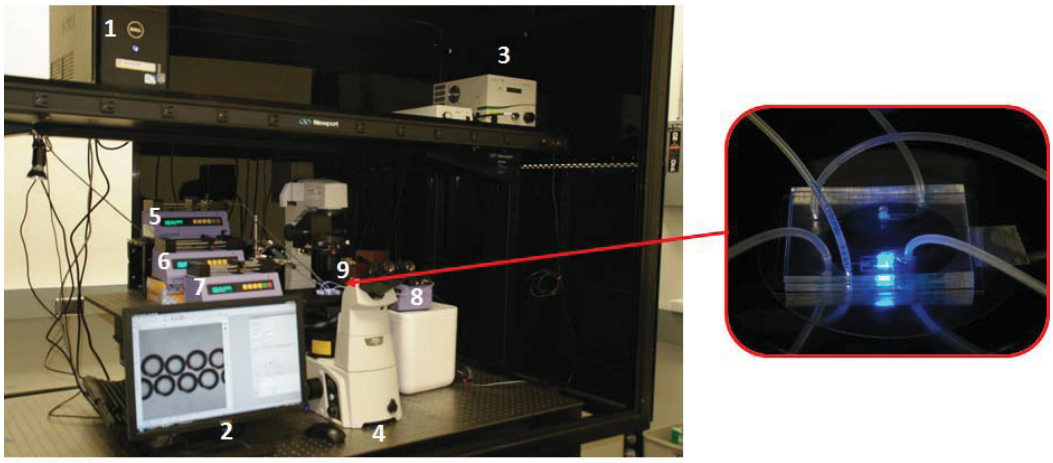

Figure 28. System setup for collagen microspheres generation. 1: computer, 2: monitor, 3: fluorescence light source, 4: inverted microscope, 5-8: syringe pumps to deliver each solution, 9: rotary pump for oil extraction.

4.9 Results and Discussion

4.9.1 Collagen Microspheres Diameter Analysis

Figure 29 and Table 4 summarize the capabilities of the device to produce monodisperse collagen microdroplets with controlled sizes. To achieve different sizes, the collagen solution flow rate was fixed at 3 μL/min while mineral oil flow rate was varied. As shown in Figure 29, monodisperse droplets were formed at each oil flow rate with the diameter linearly decreasing from 306.82 ± 1.78 μm to 103.26 ± 1.2 μm as the oil flow rate was increased from 10 to 50 μL/min. In addition to decreasing droplet size, increasing the oil flow rate also increased the rate of droplet generation (Figure 30).

Table 4. Summary of collagen droplet size at each oil flow rate.

	Oil Flow Rate (μL/min)				
	10	20	30	40	50
Size of droplets	306.82±1.78	250.10±1.73	205.04±1.93	150.14±1.98	103.26±1.20

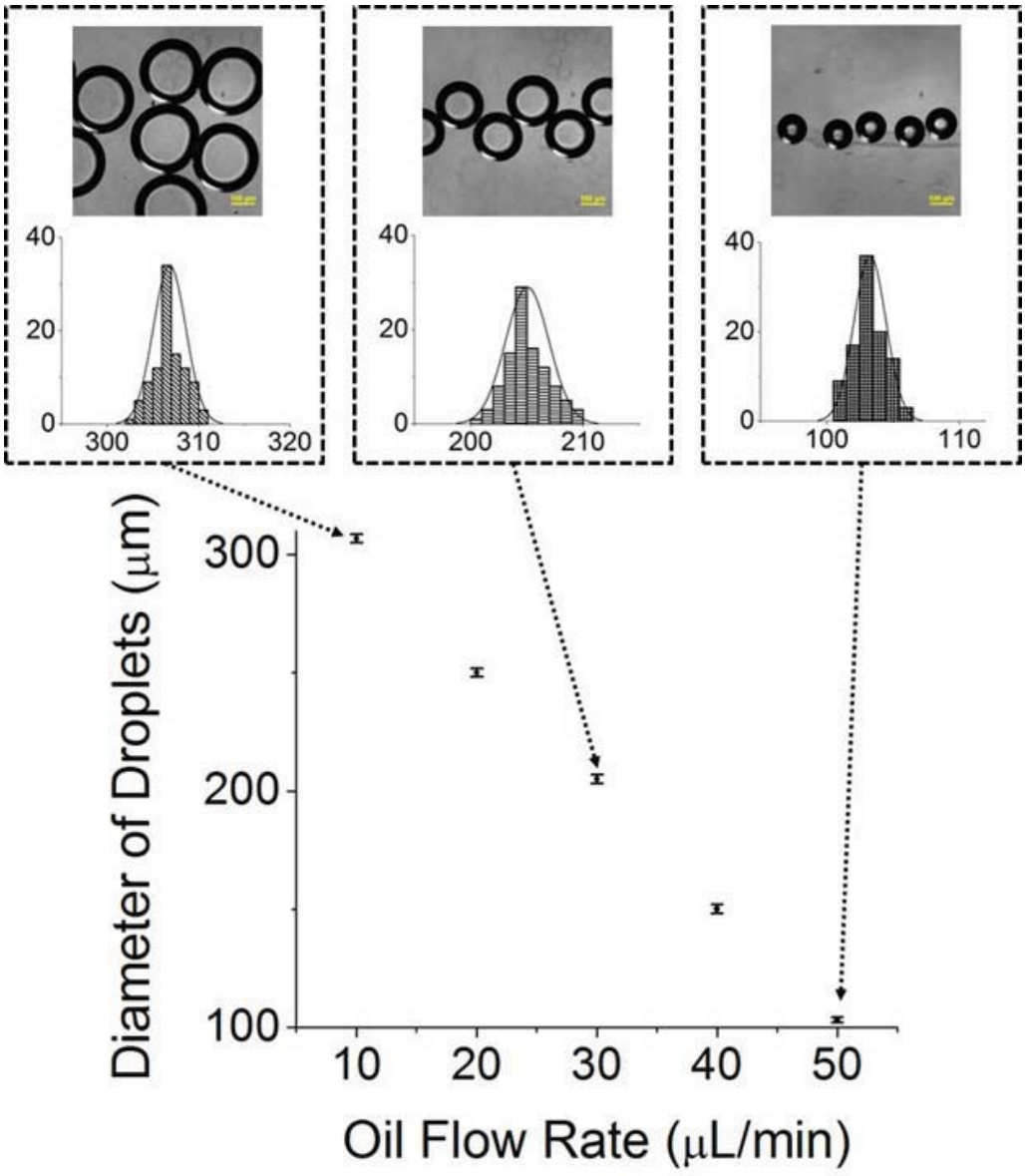

Figure 29. Effect of oil flow rate on droplet diameter. Upper: optical images size distributions of droplets generated with mineral oil flow rate of 10, 30, and 50 μL/min (while collagen flow rate was fixed at 3 μL/min). Lower: droplet diameter decreases with increasing oil flow rate.

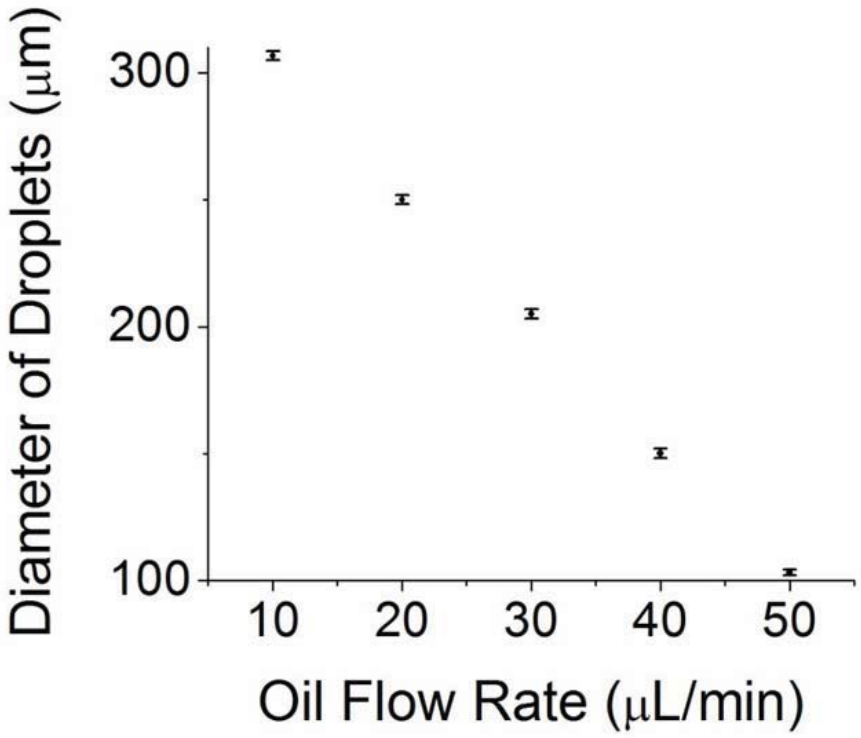

Figure 30. Collagen microspheres characterization. Droplet generation rate (droplets per minute) increases with increasing oil flow rate.

4.9.2 Cells Encapsulated in Collagen Microspheres

Collagen-cell solutions were prepared with a range of concentrations of MDA 231 cells. The flow rates of collagen and oil were set as 3 and 30μL/min, respectively, resulting in 200 μm diameter collagen droplets. The average number of cells encapsulated in collagen microspheres was 107±23 at a concentration of 1×10^8 cells/mL. When the cell concentration was lower than 1×10^5 cells/mL, single cell was encapsulated (some of the droplet had no cell and empty droplets were not counted), and multiple cells were captured at the higher concentration (Figure 31).

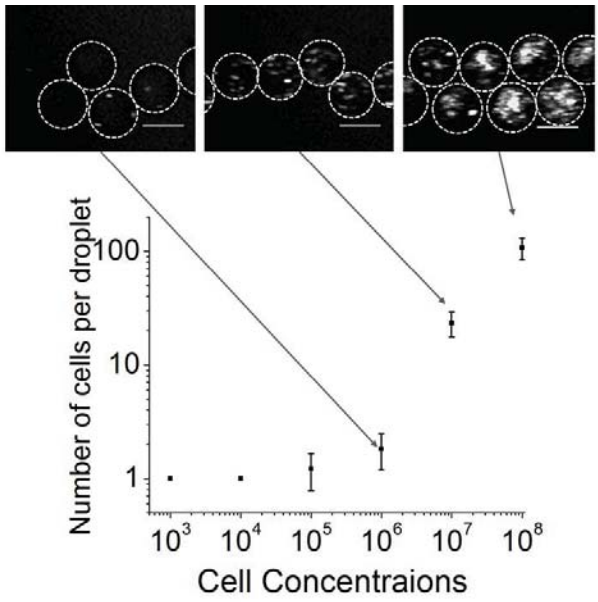

Figure 31. The analysis of MDA 231 cell encapsulation rate. Upper: Fluorescence images of GFP-expressing cells in collagen microspheres (scale bar: 200 μm). Lower: Summary plot of encapsulated cell number per sphere at different cell concentrations in the cell-collagen solution.

4.9.3 Collagen Gelation at Different Incubation Temperatures

Collagen fiber configuration may affect incorporated cell viability and proliferation. In order to verify collagen gelation in a microfluidic chip, collagen droplets were gelled at different temperatures (4, 25, and 37°C). The collagen droplets generated with each condition were collected on a sterile petri-dish and collagen fibrils were imaged by confocal reflection microscope using a 60× water immersion lens. As shown in Figure 32, no collagen fibers were observed in microspheres gelled at 4°C, while only a small number of fibers were observed when the gelation temperature was increased to 25 °C. At 37°C, collagen fibers were readily apparent.

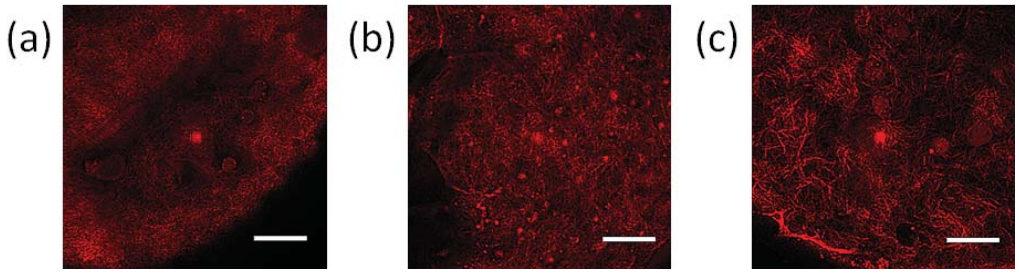

Figure 32. Fluorescence images of collagen fiber at different incubation temperatures. (a) Incubation at 4°C. (b) Incubation at 25°C. (c) Incubation at 37°C. The bright dot in the center of the image is an artifact of confocal reflectance. Scale bar: 5 μm.

4.9.4 Collagen Microspheres Formation and Throughput

As mentioned previously, the microfluidic platform was able to produce microdroplets with diameters ranging from 50 μm to 300 μm with standard deviations of ~2% at each size. The highest production rate was 200 droplets per minutes while applying a low oil flow rate, though the production rate can be easily increased by increasing the oil and aqueous flow rates.

In our microfluidic platform, collagen gelation occurred immediately after the droplet generation process. Figure 33 shows bright-field microscopy images and diameter distributions of collagen microdroplets and resulting microspheres, illustrating that the collagen microsphere diameter decreased after gelation. Diameter distributions among 100 microspheres before and after gelation in the microfluidic chip were also shown in Figure 33. Dotted line in the microscope image on the upper right side showed the original dimension of collagen microdroplet before gelation process. A ~6% reduction in diameter of collagen microspheres was observed after gelation. The final average diameter of the collagen microspheres was 272 ± 12.6 μm.

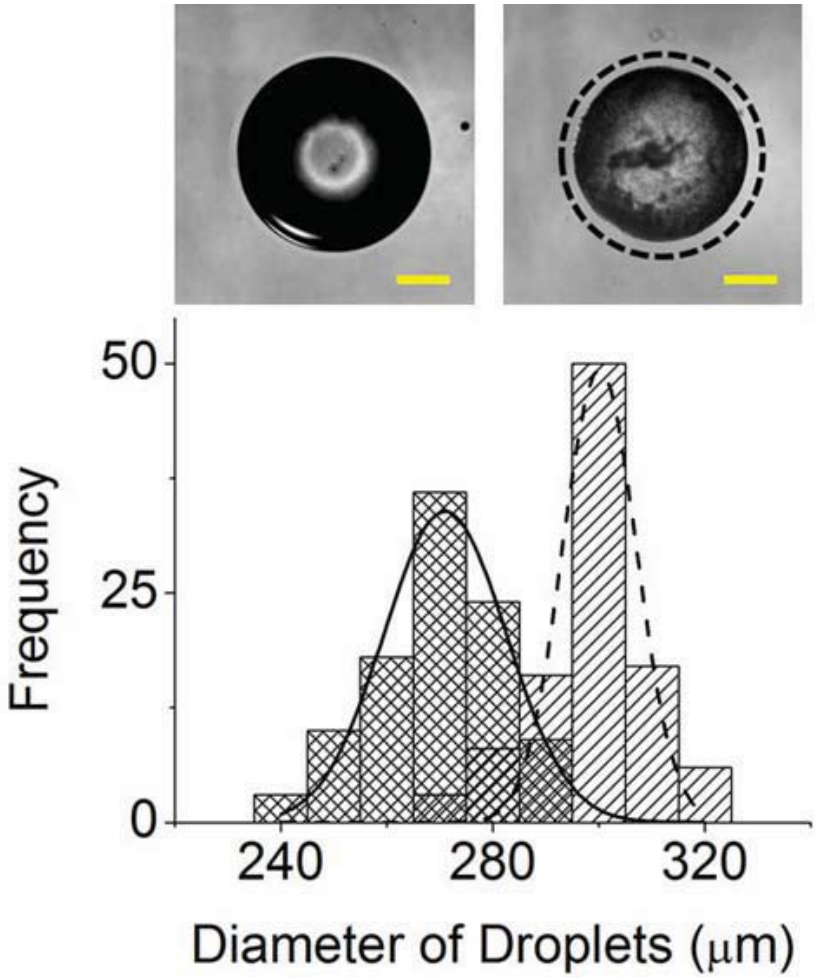

Figure 33. Diameter changes of collagen microdroplets before and after gelation. Scale bar: 100 μm.

4.9.5 Microfluidic Platform and Conventional Methods

A major advantage of our microfluidic platform over other existing methods for generating collagen microspheres is that collagen gelation takes place in confined structures immediately after droplet formation. This process avoids microsphere coalescence. Figure 34 shows a comparison of collagen microspheres generated by the microfluidic chip (collected at the extraction chamber) and a conventional emulsification approach in a test tube.[115-117] While the microspheres generated in the chip were uniform, the diameters of collagen microspheres generated by emulsification were not since multiple collagen microspheres often coalesced to form larger spheres. Evidently, collagen gelation immediately after droplet generation in the chip results in virtually no coalescence among microdroplets.

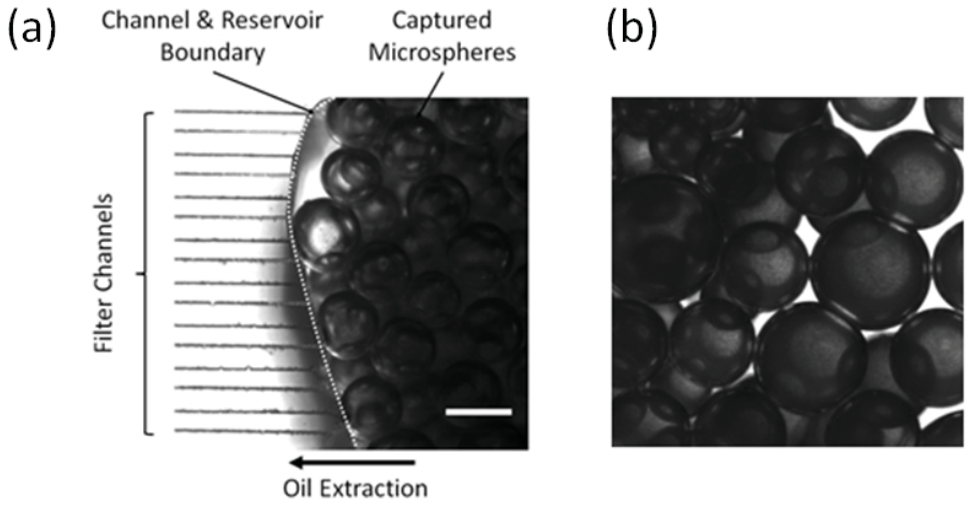

Figure 34. A comparison of collagen microspheres generated by our microfluidic chip (a) and in mineral oil made by emulsification (b). Scale bar: 200 μm.

4.9.6 Microdroplet Deformations by Centrifugation

We have observed deformation and collapse of collagen microspheres when they are extracted by centrifugation. As shown in Figure 35, deformed and agglomerated collagen microspheres were found after centrifugation process at the speed of 3000 rpm/min for 15 min, which is a typical speed and duration of centrifugation employed to separate collagen microspheres from the oil phase.

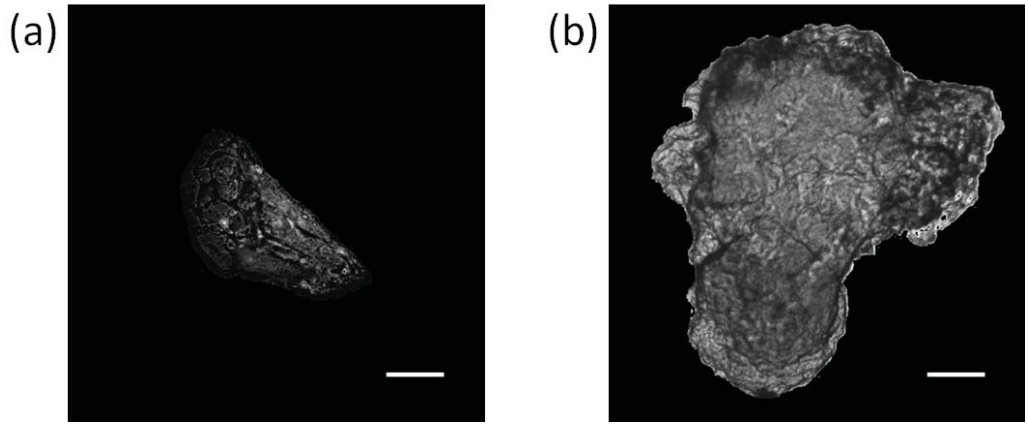

Figure 35. Optical images of malformed collagen microspheres. (a) Shape deformation of a single microsphere. (b) Agglomeration of multiple microspheres.

4.9.7 Encapsulated Cell Viability and Proliferation

The cell viability in microspheres generated within the chip and via emulsification-centrifugation was compared. As shown in Figure 36, the amount of GFP fluorescence in collagen microspheres after extraction by our approach was about 93%, compared to 48% by centrifugation, indicating a significant difference in cell viability. This difference is likely attributable to the high compressive force cells experience during centrifugation which results in collapse of at least some collagen microspheres as previously shown in Figure 35.

To characterize the fate of the encapsulated cells, we quantified changes in GFP fluorescence intensity over time. GFP-expressing MDA 231 cells encapsulated in collage microspheres with diameters of 300 μm diameters were generated by the microfluidic platform and by the conventional centrifugation method. All microdroplets made by both approaches were incubated in culture media at 37° in a 5% CO2 environment. Fluorescent images of these samples as a function of time were shown in Figure 37 (a).The fluorescence intensities of cells in microspheres as a function of time were shown in Figure 37 (b). It was evident that the numbers of cells in both samples increased, strongly indicating that MDA 231 cells were viable in microspheres generated by the microfluidic platform. The proliferation of cells in microspheres generated by our approach was substantially more rapid than those in microspheres generated by the conventional extraction method.

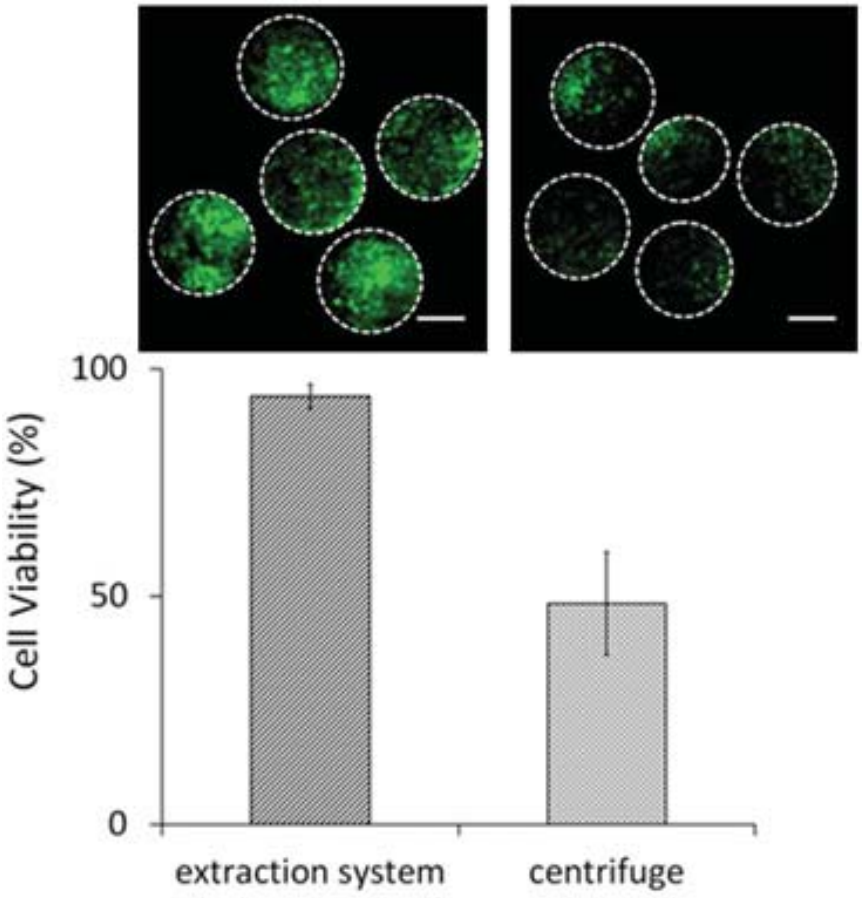

Figure 36. Fate of cells encapsulated in collagen microspheres. Upper: Fluorescent images of microspheres extracted in the microfluidic chip (left) and by centrifugation (right). Lower: Cell viability rates in 100 microspheres extracted by the two methods are summarized based on their fluorescence intensities.

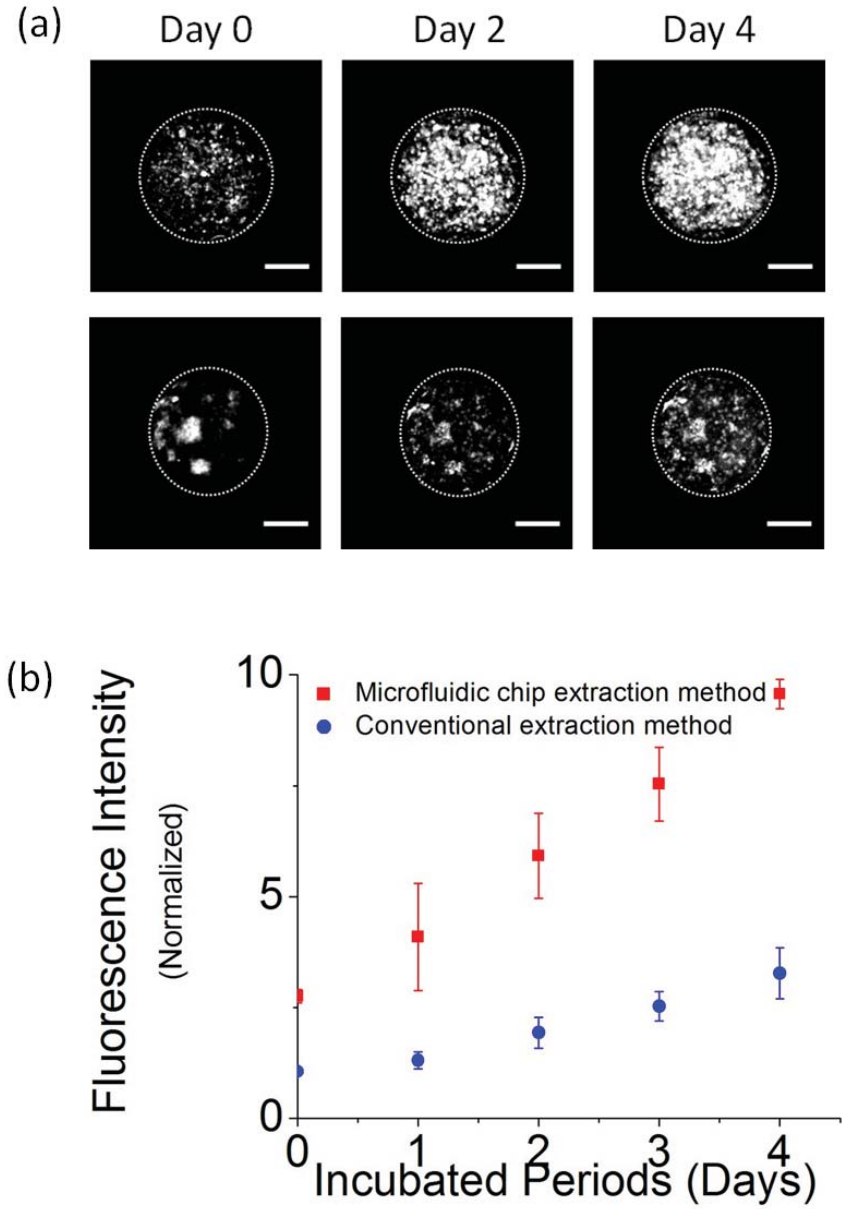

Figure 37. Encapsulated cell viability and proliferation (a) Fluorescent images of collagen microspheres encapsulated with MDA 231 cells by our method and conventional extraction method as function of time. Upper: Microspheres generated by the microfluidic platform (scale bar: 100 μm). Bottom: Microspheres generated by the conventional centrifugation (scale bar: 100 μm). (b) Fluorescence intensities in microspheres as a function of time.

5. CONCLUSIONS AND SUMMARY

We have developed the microfluidic 3D hydrodynamic flow focusing device and determined the concentrations of QD525-antibodies and QD525/HA-MAX by using the confocal single molecule detection system. The 3D hydrodynamic flow focusing could compress an analyte stream and formed a triangular cross sectional profile with sharp top angle, which could not be achieved by the conventional flow focusing methods. Since the width of the analyte flow was compressed three dimensionally to 0.3 μm at the top of triangular shaped analyte stream by the sheath flow, it could be filled inside of laser beam path. As a result, Gaussian photon burst histograms were obtained for each analyte. The number of analytes obtained from Gaussian photon burst histograms, detection volume and flow rate, the concentration of analyte were determined. Currently, it is very difficult to determine the concentration of proteins directly from biological sample such as cancer cells. This approach provided a novel method to determine the concentration of target proteins that requires only 1 minute analysis time for each sample, which is greatly improved in comparing with conventional IP/Western blot or Liquid Chromatography.

The diffusion coefficients of GFP-p53 in live HeLa cells have successfully measured by using commercial confocal microscope to RICS analysis method. RICS is able to measure protein diffusion in live cells using regular confocal microscope and require relatively short period of time. Therefore, it may be applied to a large-scale, high throughput drug screening based on the activation or inactivation of tumor suppressors or oncogene products in the future.

A microfluidic material processing platform has developed to generate collagen microspheres with encapsulated cells. Droplet generation, gelation and extraction were integrated into a single chip. Importantly, microdroplets were gelled immediately after their generation, which significantly improved microsphere dimension uniformity. In addition, our microfluidic extraction approach resulted in greater cell viability compared to that in microspheres extracted by the conventional centrifugation approach. High cell viability and uniformity of collagen microspheres demonstrated by our microfluidic platform will facilitate the development of the next generation of biomedical cell delivery or tissue engineering applications in the near future.

REFERENCES

1. L. A. Gloeckler Ries, M. E. Reichman, D. R. Lewis, B. F. Hankey and B. K. Edwards, The Oncologist **8** (6), 541-552 (2003).

2. J. Momand, H.-H. Wu and G. Dasgupta, Gene **242** (1–2), 15-29 (2000).

3. M. S. Colman, C. A. Afshari and J. C. Barrett, Mutation Research/Reviews in Mutation Research **462** (2–3), 179-188 (2000).

4. p. d. i. A. Berg van den, in *IBC Library Series "Biological Molecules in Nanotechnology: The Convergence of Biotechnology, Polymer Chemistry, and Materials Science"* (1998), pp. 123-132.

5. P. S. Dittrich, K. Tachikawa and A. Manz, Analytical Chemistry **78** (12), 3887-3908 (2006).

6. E. A. Lipman, B. Schuler, O. Bakajin and W. A. Eaton, Science **301** (5637), 1233-1235 (2003).

7. M. M. Wang, E. Tu, D. E. Raymond, J. M. Yang, H. Zhang, N. Hagen, B. Dees, E. M. Mercer, A. H. Forster, I. Kariv, P. J. Marchand and W. F. Butler, Nat Biotech **23** (1), 83-87 (2005).

8. S. Takayama, J. C. McDonald, E. Ostuni, M. N. Liang, P. J. A. Kenis, R. F. Ismagilov and G. M. Whitesides, Proceedings of the National Academy of Sciences of the United States of America **96** (10), 5545-5548 (1999).

9. R. Mehrotra, N. Jing and J. Kameoka, Applied Physics Letters **92** (21), 213109 (2008).

10. I. R. P.-N. A. Wolff, U. D. Larsen, P. Friis, G. Goranovic, C. R. Poulsen, J. P. Kutter and P. Telleman, Lab on a Chip **3**, 22-27 (2003).

11. G. Hairer, G. S. Pärr, P. Svasek, A. Jachimowicz and M. J. Vellekoop, Sensors and Actuators B: Chemical **132** (2), 518-524 (2008).

12. J. T. A. Kummrow, M. Frankowski, A. Tuchscheerer, H. Yildirim, K. Brattke, M. Schmidt and J. Neukammer, Lab Chip **9**, 972 - 981 (2009).

13. D. S. Kim, K. Han and W. Yang, Microelectronic Engineering **86** (4-6), 1343-1346 (2009).

14. J. C. Fister, S. C. Jacobson, L. M. Davis and J. M. Ramsey, Analytical Chemistry **70** (3), 431-437 (1998).

15. J. R. Webster, M. A. Burns, D. T. Burke and C. H. Mastrangelo, Analytical Chemistry **73** (7), 1622-1626 (2001).

16. M. L. Chabinyc, D. T. Chiu, J. C. McDonald, A. D. Stroock, J. F. Christian, A. M. Karger and G. M. Whitesides, Analytical Chemistry **73** (18), 4491-4498 (2001).

17. A. C. Lagerkvist, Z. Földes-Papp, M. A. A. Persson and R. Rigler, Protein Science **10** (8), 1522-1528 (2001).

18. Y. Zhang, J. T. Bahns, Q. Jin, R. Divan and L. Chen, Analytical Biochemistry **356** (2), 161-170 (2006).

19. T. G. Henares, F. Mizutani and H. Hisamoto, Analytica Chimica Acta **611** (1), 17-30 (2008).

20. B. B. Haab and R. A. Mathies, Anal. Chem. **67** (18), 3253-3260 (1995).

21. A. Van Orden, R. A. Keller and W. P. Ambrose, Analytical Chemistry **72** (1), 37-41 (1999).

22. M. Foquet, J. Korlach, W. Zipfel, W. W. Webb and H. G. Craighead, Anal. Chem. **74** (6), 1415-1422 (2002).

23. C.-K. Chou, N. Jing, H. Yamaguchi, P.-H. Tsou, H.-H. Lee, C.-T. Chen, Y.-N. Wang, S. Hong, C. Su, J. Kameoka and M.-C. Hung, Lab Chip **10** (14), 1793-1798 (2010).

24. C.-K. Chou, N. Jing, H. Yamaguchi, P.-H. Tsou, H.-H. Lee, C.-T. Chen, Y.-N. Wang, S. Hong, C. Su, J. Kameoka and M.-C. Hung, Analyst **135** (11), 2907-2912 (2010).

25. E. Brooks Shera, N. K. Seitzinger, L. M. Davis, R. A. Keller and S. A. Soper, Chem. Phys. Lett. **174** (6), 553-557 (1990).

26. S. A. Soper, E. B. Shera, J. C. Martin, J. H. Jett, J. H. Hahn, H. L. Nutter and R. A. Keller, Anal. Chem. **63** (5), 432-437 (1991).

27. P. M. Goodwin, W. P. Ambrose and R. A. Keller, Acc. Chem. Res. **29** (12), 607-613 (1996).

28. L. L. Kish, J. Kameoka, C. G. Granqvist and L. B. Kish, Applied Physics Letters **99** (14), 143121-143123 (2011).

29. A. J. de Mello and J. B. Edel, Journal of Applied Physics **101** (8), 084903-084903-084908 (2007).

30. T.-H. Wang, Y. Peng, C. Zhang, P. K. Wong and C.-M. Ho, Journal of the American Chemical Society **127** (15), 5354-5359 (2005).

31. R. F. Ismagilov, A. D. Stroock, P. J. A. Kenis, G. Whitesides and H. A. Stone, Applied Physics Letters **76** (17), 2376-2378 (2000).

32. C. Simonnet and A. Groisman, Applied Physics Letters **87** (11), 114104-114103 (2005).

33. P. S. Dittrich and P. Schwille, Analytical Chemistry **74** (17), 4472-4479 (2002).

34. C. V. Dang, Molecular and Cellular Biology **19** (1), 1-11 (1999).

35. J. H. Patel, A. P. Loboda, M. K. Showe, L. C. Showe and S. B. McMahon, Nat Rev Cancer **4** (7), 562-568 (2004).

36. J. B. Knight, A. Vishwanath, J. P. Brody and R. H. Austin, Physical Review Letters **80** (17), 3863-3866 (1998).

37. T. Stiles, R. Fallon, T. Vestad, J. Oakey, D. W. M. Marr, J. Squier and R. Jimenez, Microfluidics and Nanofluidics **1** (3), 280-283 (2005).

38. L. Gwo-Bin, C. Chih-Chang, H. Sung-Bin and Y. Ruey-Jen, Journal of Micromechanics and Microengineering **16** (5), 1024 (2006).

39. P. B. Howell Jr, J. P. Golden, L. R. Hilliard, J. S. Erickson, D. R. Mott and F. S. Ligler, Lab on a Chip **8** (7), 1097-1103 (2008).

40. J. R. W. a. T. J. H. q. q. q. Xiaole Mao, Lab on a Chip **7**, 1260-1262 (2007).

41. R. Scott, P. Sethu and C. K. Harnett, Review of Scientific Instruments **79** (4), 046104-046103 (2008).

42. C.-H. Tsai, H.-H. Hou and L.-M. Fu, Microfluidics and Nanofluidics **5** (6), 827-836 (2008).

43. N. Watkins, B. M. Venkatesan, M. Toner, W. Rodriguez and R. Bashir, Lab on a Chip **9** (22), 3177-3184 (2009).

44. M. G. Lee, S. Choi and J.-K. Park, Lab on a Chip **9** (21), 3155-3160 (2009).

45. S. Hironobu, S. Yutaka, Y. Daisuke, S. Tetsushi and S. Shuichi, Journal of Micromechanics and Microengineering **17** (11), 2211 (2007).

46. N. Sundararajan, M. S. Pio, L. P. Lee and A. A. Berlin, Microelectromechanical Systems, Journal of **13** (4), 559-567 (2004).

47. X. Mao, S.-C. S. Lin, C. Dong and T. J. Huang, Lab on a Chip **9** (11), 1583-1589 (2009).

48. G. M. Whitesides, E. Ostuni, S. Takayama, X. Jiang and D. E. Ingber, Annual Review of Biomedical Engineering **3** (1), 335-373 (2001).

49. N. Moriya, Nuclear Instruments and Methods in Physics Research Section B: Beam Interactions with Materials and Atoms **53** (2), 208-211 (1991).

50. S. T. Hess and W. W. Webb, Biophys J. **83** (4), 2300-2317 (2002).

51. M. Leutenegger, M. Gösch, A. Perentes, P. Hoffmann, O. J. F. Martin and T. Lasser, Opt. Express **14** (2), 956-969 (2006).

52. S. RÜTtinger, V. Buschmann, B. KrÄMer, R. Erdmann, R. Macdonald and F. Koberling, Journal of Microscopy **232** (2), 343-352 (2008).

53. Y. Wu, Q. Li and X.-Z. Chen, Nat. Protocols **2** (12), 3278-3284 (2007).

54. P. Yaciuk, (2007), pp. 103-111.

55. D. Figeys, L. D. McBroom and M. F. Moran, Methods **24** (3), 230-239 (2001).

56. M. Gaudreault, M.-E. Gingras, M. Lessard, S. Leclerc and S. L. Guérin, (2009), pp. 15-35.

57. B. G. Hoffman and S. J. M. Jones, J Endocrinol **201** (1), 1-13 (2009).

58. K. Jaqaman, D. Loerke, M. Mettlen, H. Kuwata, S. Grinstein, S. L. Schmid and G. Danuser, Nat Methods **5** (8), 695-702 (2008).

59. D. Axelrod, D. E. Koppel, J. Schlessinger, E. Elson and W. W. Webb, Biophysical Journal **16** (9), 1055-1069 (1976).

60. P. Roy, Z. Rajfur, P. Pomorski and K. Jacobson, Nat Cell Biol **4** (4), E91-E96 (2002).

61. I. A. Demarco, A. Periasamy, C. F. Booker and R. N. Day, Nat Meth **3** (7), 519-524 (2006).

62. M. A. Digman, P. Sengupta, P. W. Wiseman, C. M. Brown, A. R. Horwitz and E. Gratton, Biophysical Journal **88** (5), L33-L36 (2005).

63. M. A. Digman, C. M. Brown, P. Sengupta, P. W. Wiseman, A. R. Horwitz and E. Gratton, Biophysical Journal **89** (2), 1317-1327 (2005).

64. C. M. Brown, R. B. Dalal, B. Hebert, M. A. Digman, A. R. Horwitz and E. Gratton, Journal of Microscopy **229** (1), 78-91 (2008).

65. M. A. Digman and E. Gratton, Microscopy Research and Technique **72** (4), 323-332 (2009).

66. K. M. Ryan, A. C. Phillips and K. H. Vousden, Current Opinion in Cell Biology **13** (3), 332-337 (2001).

67. A. M. Bode and Z. Dong, Nat Rev Cancer **4** (10), 793-805 (2004).

68. O. Laptenko and C. Prives, Cell Death Differ **13** (6), 951-961 (2006).

69. J. K. Sax and W. S. El-Deiry, Cell Death Differ **10** (4), 413-417 (2003).

70. M. Jiang, X. Yi, S. Hsu, C.-Y. Wang and Z. Dong, Am J Physiol Renal Physiol **287** (6), F1140-1147 (2004).

71. P. J. Smith, BioEssays **12** (4), 167-172 (1990).

72. H. Yamaguchi, N. T. Woods, L. G. Piluso, H.-H. Lee, J. Chen, K. N. Bhalla, A. Monteiro, X. Liu, M.-C. Hung and H.-G. Wang, Journal of Biological Chemistry **284** (17), 11171-11183 (2009).

73. J. Beechem, E. Gratton, M. Ameloot, J. Knutson and L. Brand, in *Topics in Fluorescence Spectroscopy* (2002), pp. 241-305.

74. P. Hinow, C. E. Rogers, C. E. Barbieri, J. A. Pietenpol, A. K. Kenworthy and E. DiBenedetto, Biophysical Journal **91** (1), 330-342 (2006).

75. P. Hinow, C. E. Rogers, C. E. Barbieri, J. A. Pietenpol, A. K. Kenworthy and E. DiBenedetto, **91** (1), 330-342 (2006).

76. D. P. Lane, Nature **358** (6381), 15-16 (1992).

77. L. Yen, N. Zeng-Rong, X.-L. You, S. Richard, B. C. Langton-Webster and M. A. Alaoui-Jamali, Oncogene **14** (15), 1827-1835 (1997).

78. S. A. S. Walles, R. Zhou and E. Liliemark, Cancer Letters **105** (2), 153-159 (1996).

79. K. Y. Lee and D. J. Mooney, Chemical Reviews **101** (7), 1869-1880 (2001).

80. J. L. Drury and D. J. Mooney, Biomaterials **24** (24), 4337-4351 (2003).

81. S. J. B. Garret D. Nicodemus, Tissue Eng Part B Rev. **14** (2), 149–165 (2008).

82. Y. Kimura, M. Ozeki, T. Inamoto and Y. Tabata, Biomaterials **24** (14), 2513-2521 (2003).

83. W.-G. Koh and M. Pishko, Analytical and Bioanalytical Chemistry **385** (8), 1389-1397 (2006).

84. T. Buranda, J. Huang, G. V. Ramarao, L. K. Ista, R. S. Larson, T. L. Ward, L. A. Sklar and G. P. Lopez, Langmuir **19** (5), 1654-1663 (2003).

85. M. Piyasena, R. Zeineldin, K. Fenton, T. Buranda and G. Lopez, Biointerphases **3** (2), 38-49 (2008).

86. T. T. Lau, C. Wang and D.-A. Wang, Composites Science and Technology **70** (13), 1909-1914 (2010).

87. B. P. Chan, T. Y. Hui, C. W. Yeung, J. Li, I. Mo and G. C. F. Chan, Biomaterials **28** (31), 4652-4666 (2007).

88. H. J. C. T. Abruzzo, G. G. Shengelaia, S. M. Waldrop, D. F. Kallmes, J. E. Dion, I. Constantinidis, A. Sambanis, , Radiology **220** (2), 428-435 (2001).

89. H. Shintaku, T. Kuwabara, S. Kawano, T. Suzuki, I. Kanno and H. Kotera, Microsystem Technologies **13** (8), 951-958 (2007).

90. W. Zhang and X. He, Journal of Biomechanical Engineering **131** (7), 074515-074516 (2009).

91. C.-C. Lin and K. S. Anseth, Proceedings of the National Academy of Sciences (2011).

92. B. P. Chan, T. Y. Hui, M. Y. Wong, K. H. K. Yip and G. C. F. Chan, Tissue Engineering Part C: Methods **16** (2), 225-235 (2010).

93. T.-J. Wu, H.-H. Huang, Y.-M. Hsu, S.-R. Lyu and Y. J. Wang, Biotechnology and Bioengineering **98** (3), 578-585 (2007).

94. G. A. Di Lullo, S. M. Sweeney, J. Körkkö, L. Ala-Kokko and J. D. San Antonio, Journal of Biological Chemistry **277** (6), 4223-4231 (2002).

95. J. Heino, BioEssays **29** (10), 1001-1010 (2007).

96. H.-L. Wong, M.-X. Wang, P.-T. Cheung, K.-M. Yao and B. P. Chan, Biomaterials **28** (35), 5369-5380 (2007).

97. M. Lee, A. C. Lo, P. T. Cheung, D. Wong and B. P. Chan, Biomaterials **30** (6), 1214-1221 (2009).

98. H.-W. Cheng, K. D. K. Luk, K. M. C. Cheung and B. P. Chan, Biomaterials **32** (6), 1526-1535 (2011).

99. N. Nagai, N. Kumasaka, T. Kawashima, H. Kaji, M. Nishizawa and T. Abe, Journal of Materials Science: Materials in Medicine **21** (6), 1891-1898 (2010).

100. E. Brouzes, M. Medkova, N. Savenelli, D. Marran, M. Twardowski, J. B. Hutchison, J. M. Rothberg, D. R. Link, N. Perrimon and M. L. Samuels, Proceedings of the National Academy of Sciences **106** (34), 14195-14200 (2009).

101. Y. Deng, N. Zhang, L. Zhao, X. Yu, X. Ji, W. Liu, S. Guo, K. Liu and X.-Z. Zhao, Lab on a Chip **11** (23), 4117-4121 (2011).

102. Y. T. Matsunaga, Y. Morimoto and S. Takeuchi, Advanced Materials **23** (12), H90-H94 (2011).

103. S. K. H. S.J. Moon, Y.S. Song, F. Xu, H.O. Keles, F. Manzur, S. Mikkilineni, J.W. Hong, J. Nagatomi, E. Haeggstrom, A. Khademhosseini, U. Demirci, Tissue Engineering Part C: Methods **16** (1), 157-166 (2010).

104. T. Thorsen, R. W. Roberts, F. H. Arnold and S. R. Quake, Physical Review Letters **86** (18), 4163-4166 (2001).

105. T. Nisisako, T. Torii and T. Higuchi, Lab on a Chip **2** (1), 24-26 (2002).

106. S. L. Anna, N. Bontoux and H. A. Stone, Applied Physics Letters **82** (3), 364-366 (2003).

107. D. Chakraborty and S. Chakraborty, Applied Physics Letters **97** (23), 234103-234103 (2010).

108. G. M. Whitesides, Nature **442** (7101), 368-373 (2006).

109. Y. Murakami, T. Arakawa, E. H. Jeong, J. S. Go and S. Shoji, presented at the Solid-State Sensors, Actuators and Microsystems Conference, 2007. TRANSDUCERS 2007. International, 2007 (unpublished).

110. K. M. Choi and J. A. Rogers, Journal of the American Chemical Society **125** (14), 4060-4061 (2003).

111. X.-M. Zhao, Y. Xia and G. M. Whitesides, Journal of Materials Chemistry **7** (7), 1069-1074 (1997).

112. H. Kang, K. J. Bayless and R. Kaunas, American Journal of Physiology - Heart and Circulatory Physiology **295** (5), H2087-H2097 (2008).

113. K. J. Bayless and G. E. Davis, Biochemical and Biophysical Research Communications **312** (4), 903-913 (2003).

114. G. E. Davis and C. W. Camarillo, Experimental Cell Research **224** (1), 39-51 (1996).

115. K. Shiga, N. Muramatsu and T. Kondo, Journal of Pharmacy and Pharmacology **48** (9), 891-895 (1996).

116. Y. M. Ju, B. Yu, L. West, Y. Moussy and F. Moussy, Journal of Biomedical Materials Research Part A **93A** (1), 200-210 (2010).

117. Z. Peng, Z. Li, Y. Shen, F. Zhang and X. Peng, Polymer-Plastics Technology and Engineering **51** (7), 739-743 (2012).

APPENDIX A

Detailed process flow for 3D hydrodynamic microfluidic device for rapid protein concentration analysis.

(a)

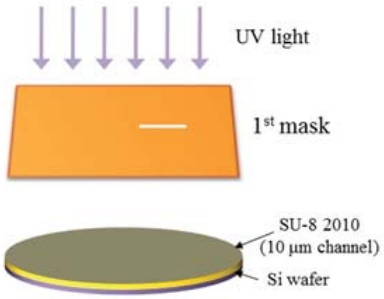

Spin coat SU-8 2010 at 3000 rpm for 30 sec (10 µm thickness) and UV expose

(b)

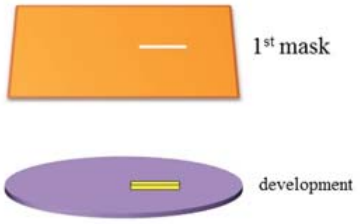

shallow channel was formed

(c)

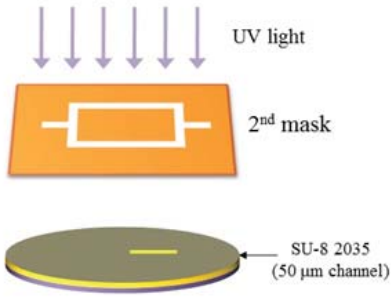

Spin coat SU-8 2050 at 3000 rpm for 30 sec (50 µm thickness) and UV expose

(d)

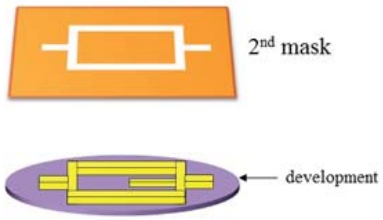

Deep channel was formed

(e)

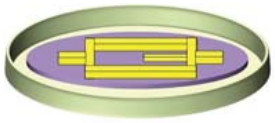

micro-mold was attached

(f)

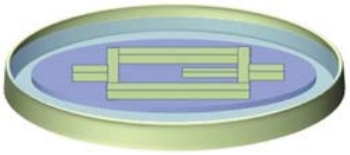

Uncured PDMS mixture was dispensed over the silicon mold

(g)

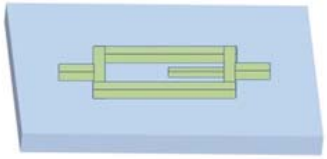

Cured PDMS was peeled off from the master silicon mold

(h)

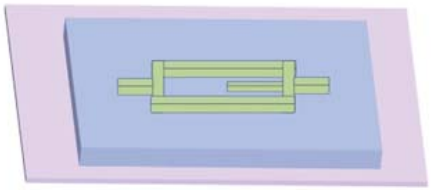

Bonded to glass slide (170μm thickness) by oxygen plasma treatment

APPENDIX B

Confocal microscope setting for Raster Image Correlation Spectroscope (RICS).

1. Objective lens: 60X water immersion lens
2. Pixel dwell time: 12.5 μs
3. Line time: 4.325 ms
4. Frame time: 1.150 s
5. Pixel size: 0.05 μm
6. Beam radius (ω): 0.2 μm
7. All images were taken at 170 μm above the cover slip

VITA

Name: Sung Min Hong

Address: Department of Electrical Engineering, Texas A&M University
College Station, TX 77843-3128

Email Address: smhong@tamu.edu

Education:
B.S., Chemical Engineering,
Kyung Hee University, February, 2002
M.S., Medical Engineering,
Graduate School of East-West Medical Science,
Kyung Hee University, February, 2004
Ph.D., Electrical Engineering,
Texas A&M University, August, 2012

Selected Publications:

1. **Sungmin Hong**, Hui-Ju Hsu, Roland Kaunas, Jun Kameoka, "Collagen microsphere production on a Chip", Lab on a Chip, accepted
2. **Sungmin Hong**, Pei-Hsiang Tsou, Choa-Kai Chou, Hirohito Yamaguchi, Chin B Su, Mien-Chie Hung, Jun Kameoka, "Microfluidic 3D hydrodynamic flow focusing for single molecule photon burst spectroscopy", Biomicrofluidics 6, 024132 (2012)
3. **Sungmin Hong**, Ying-Nai Wang, Hirohito Yamaguchi, Harinibytaraya Sreenivasappa, Chao-Kai Chou, Pei-Hsiang Tsou, Mien-Chie Hung, Jun Kameoka, "Measurement of Protein 53 diffusion constant in live HeLa Cells using Raster Image Correlation Spectroscopy (RICS)", Journal of Biomaterials and Nanotechnology (2010)
4. Chao-Kai Chou, Nan Jing, Hirohito Yamaguchi, Pei-Hsiang Tsou, Heng-Huan Lee, Chun-Te Chen, Ying-Nai Wang, **Sungmin Hong**, Chin Su, Jun Kameoka and Mien-Chie Hung, "Rapid detection of two-protein interaction with a single fluorophore by using a microfludic device," Analyst (2010)
5. **Sungmin Hong**, et al., "Impedance Measurement on a DNA Junction," Journal of Chemical Physics (2008)
   - selected for the Vir. J. Nan. Sci & Tech. Volume 127 Issue 23 Organic-Inorganic Hybrid Nanostructures (2008)
   - selected for Vir. J. Bio. Phys. Res. Volume 15 Issue 11 DNA Conformational Dynamics (2008)